Nanoscale

PAPER

View Article Online
View Journal | View Issue

Cite this: *Nanoscale*, 2026, **18**, 4419

Tunable synthesis of OH^--doped $Bi_xO_yI_z$ nanoparticles for enhanced visible-light photocatalytic degradation of water pollutants

Akshay Kulkarni, *[a] Kornelia Schlenstedt,[a] Regine Boldt, [a] Christine Steinbach,[a] Hadi Taghavian, [b] Martin Kormunda, [c] André Lerch [d] and Jochen Meier-Haack *[a]

The persistent presence of endocrine-disruptive chemicals (EDCs) in surface waters has raised serious environmental and health concerns, necessitating the development of efficient and sustainable water treatment strategies. Advanced oxidation using visible light-driven photoactive bismuth oxyiodide nanoparticles is an emerging technique for efficient water treatment. The effects of reaction parameters such as pH and temperature on the formation of semiconductor $Bi_xO_yI_z$ nanoparticles remain underemphasized despite their critical role in tailoring size, morphology, elemental composition, specific surface area, and photocatalytic activity. Accordingly, this study aimed to develop a modified solvo-hydrothermal method to optimize the synthesis of $Bi_xO_yI_z$ nanoparticles under varying pH and temperature conditions, and to establish correlations between their physicochemical properties – characterized by XRD, SEM, EDX, TEM, FTIR, UV-vis DRS, XPS, PL, Raman, and BET – and their photocatalytic performance. The results revealed that the sensitivity of iodine to pH and temperature significantly influenced particle growth and specific surface area, while the overall photocatalytic activity was also determined by the various phases of bismuth oxides and hydroxides formed during synthesis. It was demonstrated that the particles synthesized at pH values between 1.5 and 5.5 showed the highest photocatalytic activity due to the combined effect of larger surface area and interstitial surface defects formed due to hydroxylation. Finally, the possible configuration mechanism of the synthesized nanoparticles and the kinetics of photocatalytic degradation were discussed.

Received 25th September 2025,
Accepted 25th December 2025

DOI: 10.1039/d5nr04061b

rsc.li/nanoscale

1. Introduction

Pollution of surface water, which is primarily the source of drinking water, is one of the major threats that the world is currently facing. While the use of cosmetics and personal care products (PCPs) is widely regarded as one of the drivers of good quality of life,[1] these products, along with pharmaceuticals, pesticides, and fertilizers, are also the sources of contaminants of emerging concern (CECs).[2–4] Endocrine-disrupting chemicals (EDCs) like bisphenol A (BPA) are estimated to leach into the environment at over 1000 tons yearly and are found in more than 90% of tested humans.[5,6] Although pollution-treatment methods involving chlorination, ozonation, and Fenton oxidation have been proven effective through years of application, their efficiency in removing emerging contaminants is relatively poor, and their use often leads to the risk of unwanted side reactions forming hazardous by-products.[7–9]

Photocatalysis is emerging as an alternative technology in the field of water purification and shows great potential for removing various organic and inorganic pollutants.[10] Many heterogeneous semiconductor metal oxides, such as TiO_2, ZnO, CdO, Fe_2O_3, V_2O_5, *etc.*, are gaining attention from researchers worldwide. Among them, TiO_2 and ZnO nanoparticles have been studied extensively because of their chemical inertness, non-toxicity, and low cost.[9,11] However, they have relatively high bandgap energy (~3.2 eV), which limits their photoactivity within the ultraviolet region of the spectrum (λ < 380 nm).[12–14]

Bismuth oxyhalides BiOX (X = Cl, Br, I) are V–VI–VII ternary semiconductor materials that have attracted increasing interest owing to their outstanding visible-light absorption and efficient electron–hole pair separation, in addition to the pro-

[a]*Leibniz Institute of Polymer Research Dresden, Hohe Straße 6, D-01069 Dresden, Germany. E-mail: kulkarni@ipfdd.de, schlenstedt@ipfdd.de, boldt@ipfdd.de, steinbach@ipfdd.de, mhaack@ipfdd.de*
[b]*Technical University of Liberec, Institute for Nanomaterials Advanced Technologies and Innovation, Studentská 1402/2, 461 17 Liberec 1, Czech Republic. E-mail: hadi.taghavian@tul.cz*
[c]*Jan Evangelista Purkyne University, Faculty of Science, 400 96 Ústí nad Labem, Czech Republic. E-mail: martin.kormunda@ujep.cz*
[d]*TUD Dresden University of Technology, Chair Process Engineering in Hydro Systems, Bergstraße 66, 01062 Dresden, Germany. E-mail: andre.lerch@tu-dresden.de*

perties mentioned earlier.[15,16] They are crystalline in nature and exhibit a tetragonal matlockite structure. The crystal lattice consists of $[Bi_2O_2]^{2+}$ interlayers stacked between halogen-anion dual slabs along the *z*-axis, held together by van der Waals forces. This [X–Bi–O–Bi–X] structure enables the generation of an inner electric field between halogen and $[Bi_2O_2]^{2+}$ slabs, which are accountable for the valence band and conduction band of the BiOX semiconductor, respectively. The distance between the two bands narrows with increasing atomic radius of the halogen, resulting in a decrease in the bandgap energy according to the sequence BiOF > BiOCl > BiOBr > BiOI.[17–21]

Although bismuth oxyiodide exhibits the highest photoactive potential among the BiOX materials, its activity can be limited by its low conduction-band position and the high likelihood of electron–hole pair recombination. Furthermore, the activity of semiconductor photocatalysts is largely determined by their composition, morphology, surface area, and exposed facets. Thus, researchers worldwide are working on strategies for improving the photocatalytic performance of bismuth oxyiodide.[12,22] Among the many routes of BiOI synthesis, the solvo-hydrothermal method is the most popular in the scientific community. Using this process, $Bi(NO_3)_3{\cdot}5H_2O$ and KI are used as precursors, while water, ethanol, ethylene glycol, polyethylene glycol, glycerine, and nitric acid have been the solvents chosen by various research groups. The reaction mixture is heated in a Teflon-lined autoclave at 120 °C to 180 °C for 10 to 16 hours.[23,24] Yu and Han reported that BiOI prepared using ethylene glycol (EG) as the solvent shows photocatalytic properties that are superior compared to those of BiOI prepared by others.[25] Duran-Alvarez *et al.* described higher-temperature synthesis leading to a product with slightly increased porosity that does not affect the photocatalytic performance,[26] while Elamin *et al.* reported that a room-temperature sonochemical process produced good results.[27] Xiao and Zhang conducted the reaction in an open vessel, stating that the sealed conditions of an autoclave are unfavourable for gas-generating reactions.[12] Furthermore, Guin *et al.*, Long *et al.*, and Matiur *et al.* calcinated their bismuth oxyhalide up to 500 °C to obtain product with iodine-deficient phases *viz.* $Bi_4O_5I_2$, Bi_5O_7I, $Bi_7O_9I_3$.[15,28,29] Pai Wu's research group synthesized iodine-deficient $Bi_7O_9I_3$ by increasing the pH value of the reaction mixture up to 12, while the research group of Gongjaun Wu claimed iodine-deficient $Bi_7O_9I_3$ could be obtained at pH 8.[30,31] Ma *et al.* used various ratios of bismuth to iodine in the reaction mixture and reported that oxygen-deficient $Bi_7O_9I_3$ exhibits enhanced photoactivity.[32] The effect of water content on crystal growth was studied by He *et al.*, who stated that a weaker acidic environment promotes the growth of [0 0 1] facets, which are more active than [1 1 0] facets. At the same time, Pan *et al.* claimed that [1 1 0] facets can absorb a high amount of oxygen to form O_2^- and $OH^{\bullet}$ radicals and thus are more active than [0 0 1] facets.[33,34] Overall, many researchers have acknowledged the use of bismuth nitrate pentahydrate as a precursor. However, the possibility of the formation of bismuth oxides, bismuth hydroxides, and basic bismuth nitrate (BBN) compounds along with the product has been overlooked. Temperature-induced iodine loss has been reported by many researches, but reports on pH-induced iodine loss and the effects of surrounding OH^- ions in the reaction mixture (which can replace the iodine in the BiOI crystal structure) are still underrepresented. Furthermore, the summary of conducted research (Table S1, SI) indicates a lack of uniformity in the synthesis procedures and the resulting products. This inconsistency makes it challenging for new researchers or industries seeking to synthesize a customized product for specific applications to understand and use the available literature effectively.

In a quest to obtain the best photoactive product, the stepwise study on the effects of the above-mentioned parameters on particle composition, morphology, and growth has largely been overlooked and has created significant ambiguity.

In this work, we have developed a straightforward and energy-efficient approach to $Bi_xO_yI_z$ synthesis by combining solvothermal and hydrothermal procedures, resulting in a superior product in terms of photoactivity. We also addressed the ways of tailoring nanoparticles as per requirements by studying the effect of pH and temperature on their synthesis and performance. In this simple yet novel method, we synthesized $Bi_xO_yI_z$ under air conditions with EG and water as solvents. The stoichiometric ratio of bismuth to iodine was maintained at 2 : 1. The stirring speed of the reaction mixture was kept constant at 750 rpm, and NaOH was used to change the pH value from 1 to 8. The produced materials were characterized by means of several techniques such as XRD, SEM, EDX, TEM, FTIR, UV-vis DRS, XPS, PL, Raman, and BET. The photocatalytic activity of the products against colourless BPA was evaluated under the irradiation of a 50 W white LED lamp, acknowledging its thermo-economic advantages over xenon and halogen lamps.[35,36]

2. Materials and methods

2.1 Reagents

Bismuth(III) nitrate pentahydrate ($Bi(NO_3)_3{\cdot}5H_2O$, 98%, reagent grade, MW 485.07 Da) was purchased from Sigma-Aldrich GmbH and used as the bismuth source. Potassium Iodide (KI, 99+%, synthesis grade, MW 166 Da) and ethylene glycol (EG, MW 62.07 Da) were purchased from Acros Organics and Carl Roth GmbH and employed as the iodine source and solvent, respectively. Analytical grade sodium hydroxide (NaOH, MW 39.99 Da) was ordered from Honeywell-Fluka and utilised for pH variation, while bisphenol A (MW 228.29 Da) was purchased from Sigma-Aldrich GmbH and served as a colourless model pollutant. All the reagents were used as received without further purification. Deionized (DI) water was used for synthesis and washing purposes.

2.2 Synthesis

This study proposes a modified solvo-hydrothermal synthesis process in which 10 mmol (4.86 g) of $Bi(NO_3)_3{\cdot}5H_2O$ was dis-

solved in 40 mL of ethylene glycol (EG) in a round bottom flask at 70 °C and 750 rpm stirring speed using an oil bath and magnetic stirrer, respectively. 5 mmol (0.83 g) of KI solution in 150 mL of DI water was then heated to 70 °C and rapidly added to the $Bi(NO_3)_3{\cdot}5H_2O$ solution. A bright red precipitation was immediately observed in the reaction mixture, which was then stirred for a minute to ensure complete mixing and subsequently placed in an ice bath to stop the reaction. The produced slurry was then filtered, washed with DI water and finally dried in a vacuum oven at 60 °C for 24 hours. To study the effect of pH, different amounts of NaOH (7.5, 22.5, and 27.5 mmol) were dissolved in 150 mL of water and KI and rapidly added to the $Bi(NO_3)_3{\cdot}5H_2O$ solution. The colour of the precipitation changed from bright red (0 mmol NaOH) to pale yellow (27.5 mmol NaOH) as the amount of added NaOH was increased (see Table 1). To investigate the effect of temperature on the resulting precipitation, the synthesis was conducted without NaOH at 25 °C and 100 °C. Table 1 details all batch variations with their respective visible product outcomes.

2.3 Characterisation

Powder X-ray diffraction (XRD) measurements were carried out to analyse the prepared samples with regard to their impurities and crystallinity. The measurements were performed on a Bruker D8 Advance diffractometer (Billerica, MA, USA) with Cu Kα radiation (λ = 0.15406 nm) and a total acquisition time of 1800 s. The powder was placed between two acetate foils, clamped in a sample holder, and measured in transition mode. Scattered X-ray intensities were recorded using a two-dimensional Bruker VÅNTEC-500 detector (2048 × 2048-pixels). The resulting 2D patterns were azimuthally integrated over a 2θ range of 5–60° with a step size of 0.02°. Scanning electron microscopy (SEM) was performed to study particle morphology at the nanometre scale, and elemental mapping was conducted using energy-dispersive X-ray spectroscopy (EDX) at an accelerating voltage of 10 kV. A Gemini Ultra Plus microscope (Carl Zeiss Microscopy GmbH, Oberkochen, Germany) equipped with a Bruker Flat Quad X-Flash 5060F detector was used for these analyses. All samples were mounted to aluminium pin stubs using double-sided carbon adhesive tape and coated with a 3 nm platinum layer to minimize electrostatic charging. X-ray photoelectron spectroscopy (XPS) was conducted using a SPECS PHOIBOS 100 hemispherical analyzer with a 5-channel detector and a SPECS XR50 X-ray source fitted with Al/Mg dual anodes. The Al anode was operated at E-pass energies of 40 eV for survey scans and 10 eV for high-resolution spectra. The specific surface areas of the samples were evaluated by nitrogen sorption (Autosorb iQ MP, Anton Paar GmbH, Ostfildern-Scharnhausen, Germany) using the Brunauer–Emmett–Teller (BET) method. Prior to analysis, all samples were degassed at 130 °C for 24 h under ultrahigh vacuum (5×10^{-10} mbar) using an Autosorb iQ3 system. UV-vis diffuse reflectance spectroscopy (DRS) was conducted using a Cary 5000 spectrophotometer (Ulbricht Kugel) to determine the bandgap energy of the synthesized samples. Raman spectra were acquired using a WITEC alpha 300R confocal Raman system with a 532 nm laser operated at 1 mW power. Fourier transform infrared (FTIR) spectroscopy was performed using a Tensor 27 spectrometer (Bruker, Germany). Spectra were recorded from 4000 to 600 cm^{-1} with a resolution of 4 cm^{-1}, accumulating 100 scans per spectrum. Specimens for transmission electron microscopy (TEM) were prepared by dispersing the powder in water, depositing a drop of the dispersion on a carbon-coated TEM grid, and allowing it to dry. TEM images were recorded using a Libra200 instrument (Carl Zeiss Microscopy Deutschland GmbH, Oberkochen, Germany) operated at an acceleration voltage of 200 kV. Photoluminescence (PL) spectra were recorded on a Tecan Infinite M-Plex system (Tecan, Switzerland) equipped with a Tecan 12 Flat Bottom Black Cuvette holder, using an excitation wavelength of 365 nm.

Table 1 Overview of synthesized batches of BiOI

	Observations			
Sample name	Temperature (°C)	Conc. of NaOH (mmol)	pH	Colour
$BiOI_{1-70}$	70	0	1	Bright red
$BiOI_{1.5-70}$	70	7.5	1.5	Reddish-orange
$BiOI_{5.5-70}$	70	22.5	5.5	Orange
$BiOI_{8-70}$	70	27.5	8	Pale yellow
$BiOI_{1-25}$	25	0	1	Dark red
$BiOI_{1-100}$	100	0	1	Orange

2.4 Photocatalytic performance test

Determination of the photocatalytic activity of particles against BPA is an essential step toward constructing a pathway for their application-based synthesis and use. The photocatalytic activity of as-synthesized $Bi_xO_yI_z$ particles was determined by conducting photocatalytic batch experiments. These experiments were performed by keeping a beaker containing a 100 mL mixture of BPA solution (105 mg L^{-1}) and $Bi_xO_yI_z$ catalyst (1 g L^{-1}) under a black opaque plastic housing with dimensions 30 × 30 × 30 cm^3. This opaque cover is designed so that no external light irradiation is allowed to enter. The only light source for irradiation was a 50 W warm white LED lamp (TCP = 4000 K; Ledvance Enduro® Flood) that could be placed on top of the opaque cover (Fig. S1, SI). The LED lamp was switched off for the initial hour of the respective experiments to achieve adsorption equilibrium between BPA and the catalyst. Samples were extracted at regular intervals using a syringe with a hydrophobic PTFE filter cap to avoid ingression of the nanoparticles' into the samples. The concentration of BPA in the samples was then determined by UV-vis spectroscopy (Lambda 800, Perkin Elmer) at a wavelength of 276 nm. The resulting absorption values were recalculated to convert them to concentrations using a previously recorded calibration curve. The concentration values were plotted against time to assess the degradation of BPA.

Many research groups have conducted multiple runs of the experiment to determine the longevity of their synthesized particles. However, these repetitions require these particles to be washed and dried before the start of every new run, which can

be impractical for the intended continuous operation. Using these particles without drying does not guarantee the same initial concentration for each run, which may not lead to reliable results. (Fig. S2, in the SI sheet demonstrates such a test in which the initial concentration of the pollutant was normalized for each cycle. Results show a marginal drop in the photoactivity after the 4th cycle, possibly due to loss of catalyst during sampling. The XRD diffractogram of the used catalyst did not reveal any changes in the crystal structure.) Hence, in this work and to the best of our knowledge for the first time, a high initial concentration (105 mg L^{-1}) of BPA (instead of running 4–5 cycles of BPA of concentration 20 mg L^{-1}) was used to determine the photoactivity of the particles during a single run, which we believe would properly simulate the long-time continuous operation of the synthesized particles.

3. Results and discussion

3.1 Appearance, SEM, and EDX

During the synthesis, immediate precipitation was observed upon addition of the aqueous KI solution to the bismuth nitrate solution in EG, regardless of pH and temperature. However, the color of the precipitate varied with pH and temperature. The SEM images of the synthesized $Bi_xO_yI_z$ particles, which are shown in Fig. 1 and 2, include photographs as insets that illustrate their color distribution depending on the different reaction parameters.

$$2Bi(NO_3)_3 \cdot 5H_2O + 3HOCH_2CH_2OH \rightarrow Bi(OCH_2CH_2O)_3 + 6HNO_3 + 10H_2O \quad (1)$$

A bright red-coloured powder ($BiOI_{1-70}$) was obtained from the synthesis without NaOH at 70 °C. The suspension exhibited a pH value of 1 as nitric acid was formed upon dissolution of $Bi(NO_3)_3{\cdot}5H_2O$ in EG (eqn (1)).[12,37]

$$4HNO_3 \rightarrow 2H_2O + 4NO\uparrow + 3O_2\uparrow \quad (2)$$

$$8H^+ + 2NO_3^- + 6I^- \rightarrow 3I_2\uparrow + 2NO\uparrow + 4H_2O \quad (3)$$

The colour of the products faded from dark orange at pH = 1.5 ($BiOI_{1.5-70}$), to light orange at pH = 5.5 ($BiOI_{5.5-70}$) and to light yellow at pH = 8 ($BiOI_{8-70}$) with the addition of NaOH. This colour bleaching could be attributed to the loss of iodine and the formation of $Bi(OH)_3$ and basic bismuth nitrate (BBN) derivatives,[38–40] which are white in colour (Fig. S5, SI).

Furthermore, the particles synthesized at 100 °C ($BiOI_{1-100}$) also turned out to be orange in colour due to the loss of iodine as the nitric acid decomposes at higher temperatures and acts as a potent oxidising agent to oxidise I^- to I_2 (eqn (2) and (3)).[12,41,42] Purple vapours of iodine were seen evolving from the reaction mixture at 100 °C. Once I^- was consumed, Bi^{3+} reacted with O_2 to form Bi_2O_3 crystals. A similar colour pattern was also observed between the particles produced at 70 °C and 25 °C ($BiOI_{1-70}$ & $BiOI_{1-25}$), where the latter had a darker shade.

3.1.1 SEM. The morphology of the synthesized particles was studied using SEM. As shown in Fig. 1 and 2, most of the synthesis variations of $Bi_xO_yI_z$ exhibit a flowerball-like hierarchical architecture constructed from numerous straight nanosheets with thicknesses of around 16–18 nm. However, the size and shape of these flowerball-like microspheres were found to change with varying pH, and temperature.

Particles synthesized without NaOH ($BiOI_{1-70}$) formed flowerball-like microspheres of non-uniform sizes with an average diameter of 1.65 μm. These flowerballs consist of densely connected thin nanosheets and are clearly separated from each other (Fig. 1(a)). However, with an increase in pH ($BiOI_{1.5-70}$), the particles agglomerated and comprise smaller flowerballs (Fig. 1(b)). This indicates the restricted peripheral growth of flowerballs with decreasing iodine content in the product (Fig. 1(a)). A further increase in pH leads to severe agglomeration. The resulting aggregates are 10–100 μm in size and contain clusters of more petite, unrecognizable flowerballs (Fig. 1(c and d)). This formation is mainly ascribed to the production of BBN derivatives and $Bi(OH)_3$ upon addition of NaOH to the reaction mixture. These compounds largely determine the shape of aggregates that form with increasing pH (Fig. S5 SI).

Particles produced at 25 °C ($BiOI_{1-25}$) also exhibit flowerball hierarchical structures with more densely connected nanosheets than particles produced at 70 °C ($BiOI_{1-70}$) (Fig. 2 (a and b)). Meanwhile, the 100 °C synthesis ($BiOI_{1-100}$) resulted in thinner platelets (Fig. 2(c)). This phenomenon can be explained by the lowering of iodine content with increasing temperature. It can be observed that, contrary to the pH-induced iodine loss, temperature-induced iodine loss restricts the internal growth of the flowerballs.

3.1.2 EDX. The energy dispersive X-ray spectroscopy analysis of the synthesized products was conducted to evaluate their varying iodine content as a function of pH and synthesis temperature. It is known that the iodine in the product is interchangeable with OH^- ions.[30,31] Hence, as shown in Fig. 3(a), the iodine-to-bismuth ratio was used to demonstrate the change in the iodine content of the product.

A steady decrease in iodine was observed with increasing pH up to 5.5. Subsequently, the I : Bi ratio quickly dropped to a value of 0.23 under basic conditions at pH 8 due to excess OH^- ions (Fig. 3(a)). A similar sudden drop in the iodine-to-bismuth ratio was also observed with an increase in the reaction temperature from 70 °C to 100 °C (Fig. 3(a)). This is due to the temperature sensitivity of nitric acid, as demonstrated by eqn (2) and (3).

Products with low iodine content as a result of higher temperature ($BiOI_{1-100}$) contain impurities in the form of rods, as denoted by red circles in Fig. 3(b). This is possibly due to Ostwald ripening, which leads to the formation of various Bi_2O_3 structures.[43] The orange colour in Fig. 3(b) indicates the presence of bismuth, while the purple colour indicates traces of iodine. It is evident from the figure mentioned above that no iodine traces were found in the formed rods (see red circles in Fig. 3(b)). It is also important to note that no such structures were obtained in the iodine-depleted product synthesized at pH 8 ($BiOI_{8-70}$). This confirms that pH-induced iodine loss

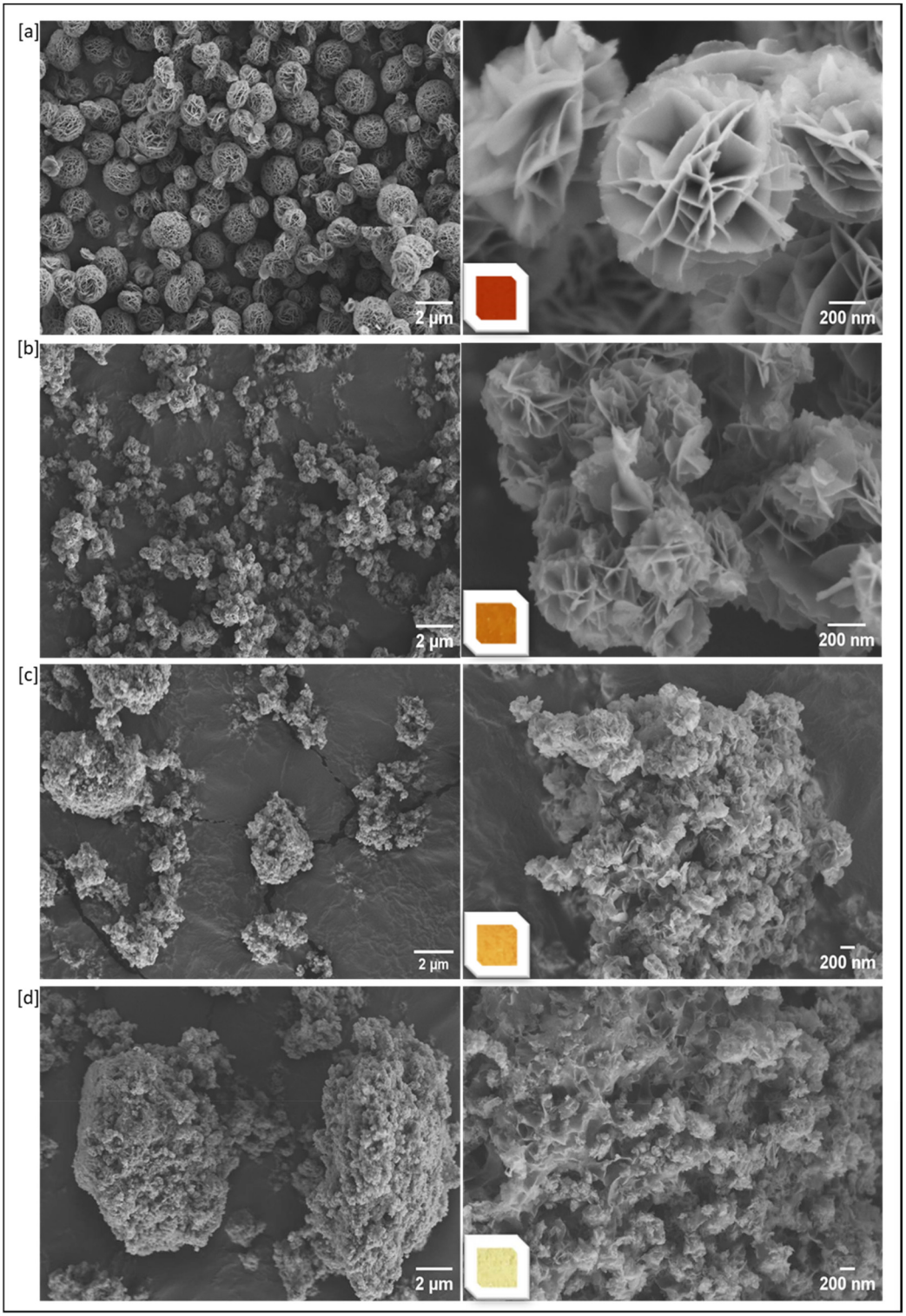

Fig. 1 SEM images (×5k (left) and ×50k (right) magnification) of the synthesized particles and their appearance with varying pH. $BiOI_{1-70}$ (a), $BiOI_{1.5-70}$ (b), $BiOI_{5.5-70}$ (c), and $BiOI_{8-70}$ (d).

has a different mechanism compared to temperature-induced iodine loss. Fig. 3(c) shows the EDX composite spectrum of $BiOI_{1-100}$. The EDX spectra of other products can be found in Fig. S6 of the SI.

3.2 XRD

All synthesized $Bi_xO_yI_z$ nanoparticles were examined for their crystalline properties using the X-ray diffraction (XRD) tech-

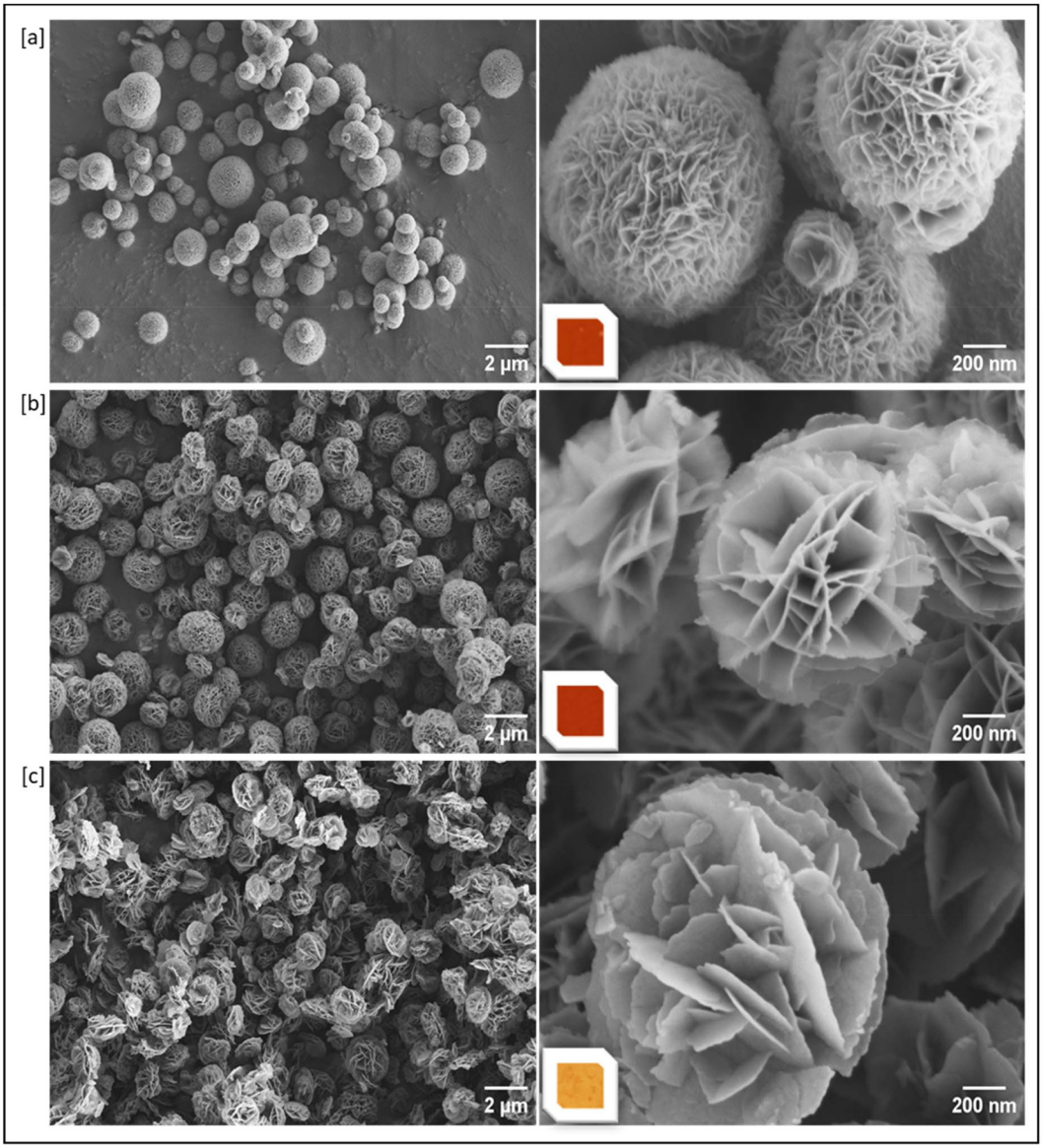

Fig. 2 SEM images (×5k (left) and ×50k (right) magnification) of the synthesized particles and their appearance with varying temperature. $BiOI_{1-25}$ (a), $BiOI_{1-70}$ (b), and $BiOI_{1-100}$ (c).

nique. Fig. 4 exhibits the diffractograms and the calculated crystallinities of the synthesized compounds. Particles synthesized at pH 1 (0 mmol NaOH) exhibit sharp and intense peaks, reflecting their crystalline nature. The diffractogram of the powder obtained at pH 1 and 70 °C ($BiOI_{1-70}$) precisely matches the reference diffractogram of BiOI (JCPDS 01-73-2062) with no other apparent impurities. However, many researchers also claim identical XRD patterns for $Bi_7O_9I_3$.[12,35] The decrease in peak sharpness with increasing pH observed in Fig. 4(a) is the result of the generation of $Bi_p(OH)_q(NO_3)_r$ by the addition of OH^- ions to the reaction mixture.[38,39] Thus, the semi-crystalline nature of $Bi_p(OH)_q(NO_3)_r$ (Fig. S3, SI) dominates the diffractogram with increasing synthesis pH. In this case, peak broadening cannot be associated with a reduction in crystallite size. Nevertheless, the crystallinity of these particles was computed by dividing the area under the peaks by the total area after baseline correction using Origin 2019 software. The calculated results show a rapid reduction in crystallinity from 91% at pH 1 to 76% at pH 1.5. However, crystallinity decreased steadily to 61% at pH 8 (Fig. 4(d)). On the other hand, no significant decrease in crystallinity was observed with increasing reaction temperature (a drop of only 7% from 91% at 70 °C to 84% at 100 °C), possibly due to the formation of Bi_2O_3 crystals (see EDX analysis, Fig. 3(b)).

The peak-widening phenomenon occurs with decreasing synthesis temperature (Fig. 4(c)), which can be attributed to the diminishing crystal size (because no OH^- ions were added

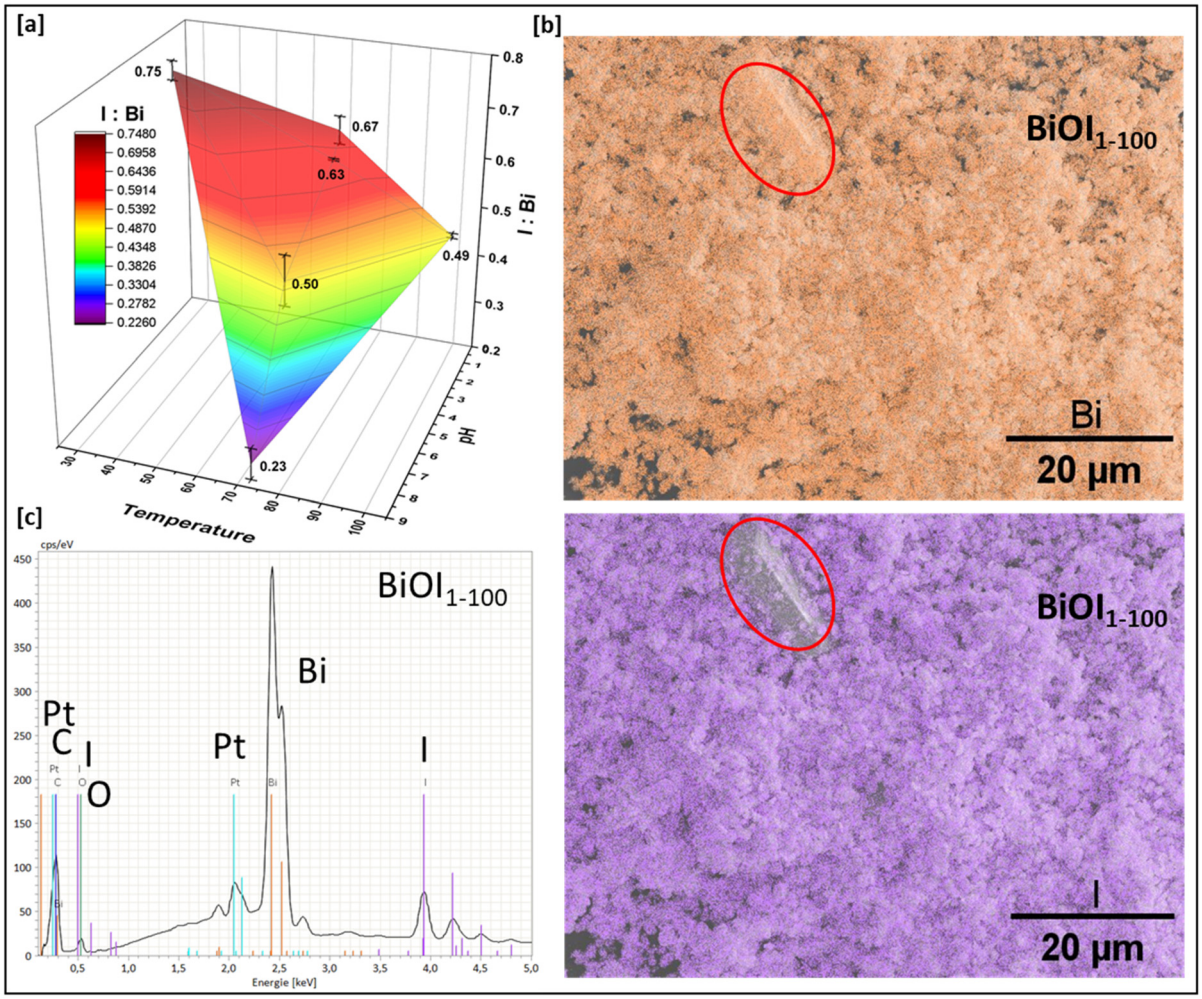

Fig. 3 Iodine-to-bismuth ratios in synthesized compounds (a). EDX mapping of formed structures (bismuth in orange and iodine in purple; red circles highlight the presence of bismuth and lack of iodine in the formed rods) in $BiOI_{1-100}$ (b). EDX composite spectrum of $BiOI_{1-100}$ (c).

to the reaction mixture). As shown below, Scherrer's equation was used to calculate the average crystal size:

$$L = \frac{K \times \lambda}{\beta \cos \theta}$$

where L is the crystal size (nm), K is the shape factor (= 0.9), λ is the X-ray wavelength (= 0.15406 nm), β is the full width at half maximum (FWHM) of the peak (radians) and θ is the Bragg angle (radians). A linear increase in average crystal size was observed from 6.77 nm in the case of $BiOI_{1-25}$ to 10.1 nm for $BiOI_{1-70}$, and finally to 11.3 nm for $BiOI_{1-100}$ with increasing reaction temperature. Moreover, the gap between the [0 1 2] and [1 1 0] peaks has also widened (Fig. 4(b)) with increasing pH. This can be attributed to the development of lattice strain in the crystal structure affecting its size[44] and forming interstitial site defects with additional bismuth and oxygen atoms in the BiOI crystal structure, which has been confirmed by other reports focused on iodine-deficient bismuth oxyiodides.[45] The relative peak intensities of [1 1 0] planes and [0 0 1] planes to [0 1 2] planes of the prepared samples are compared and their trends with increasing pH and temperature are also illustrated (Fig. S4, SI).

3.3 BET surface area

The specific surface area of the catalyst directly affects its performance. Thus, it is essential to assess the impact of varying pH and temperature of synthesis on the specific surface area (S_{BET}) and pore diameter (D_p) of the products. Nitrogen adsorption–desorption isotherms were analysed using the BET method for specific surface area measurements, and density functional theory (DFT) was applied to evaluate the pore size distribution of particles. Because of their flowerball hierarchical structure, as-obtained $Bi_xO_yI_z$ particles possess a large surface area. The relationships of specific surface area (S_{BET}) with variations in synthesis parameters are depicted in Fig. 5(a). A steady increase in S_{BET} from 12 $m^2\ g^{-1}$ to 63 $m^2\ g^{-1}$ was observed with increasing synthesis pH. A negative trend in S_{BET} was observed with increasing temperature. In the case of temperature variation, the S_{BET} of the powder dropped quickly from 34 $m^2\ g^{-1}$ (25 °C) to 12 $m^2\ g^{-1}$ (70 °C), after which no

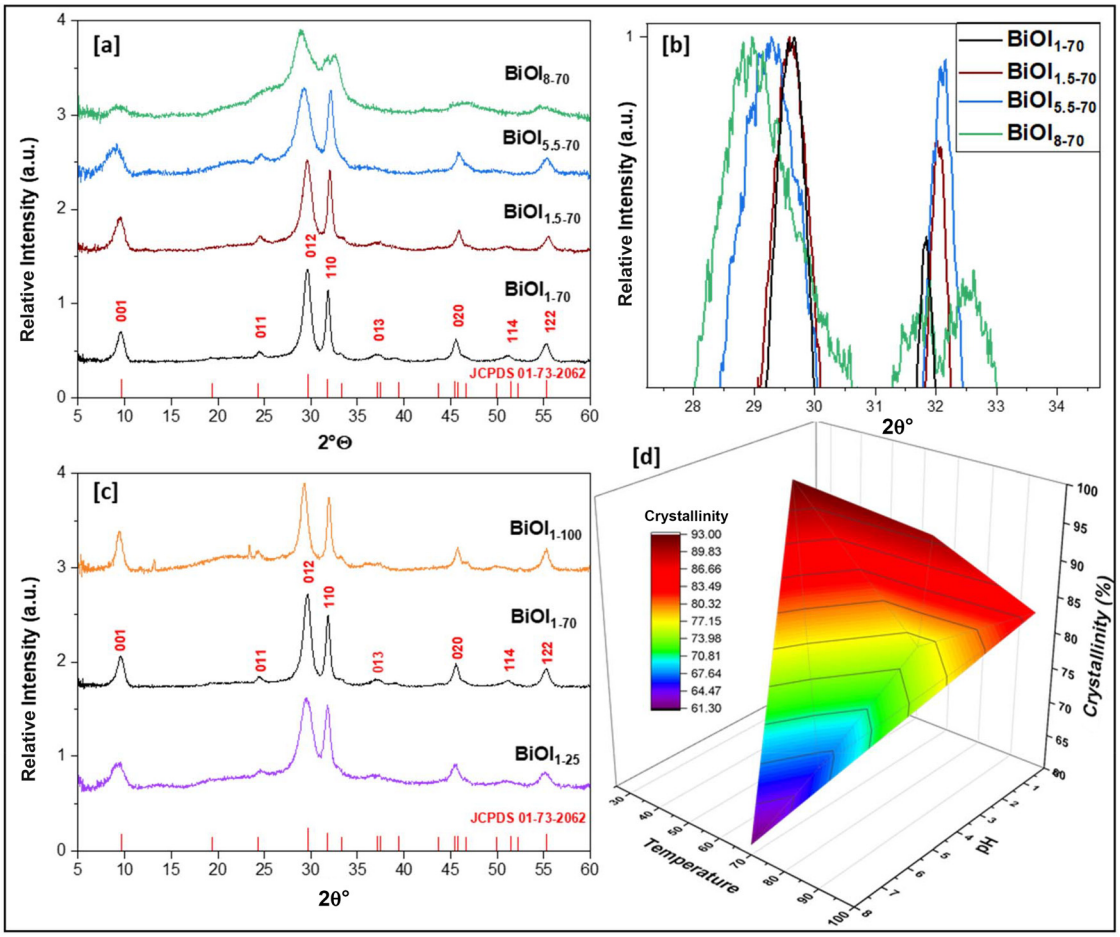

Fig. 4 Diffractograms of the synthesized products (a, b, and c), and crystallinity with respect to pH and temperature (d).

further significant decrease in S_{BET} was observed. Every synthesis procedure except the one carried out at room temperature ($BiOI_{1-25}$) yielded products with macroporous or nonporous structures (Fig. 5(b) and (c)). Particles produced at 25 °C show type IV adsorption isotherms with H3 desorption hysteresis loop and exhibit mesopores with sizes ranging from 4–6 nm and 8–14 nm, respectively (Fig. 5(d)). The hysteresis profile indicates non-rigid aggregates with platelet-like structures fostering slit-shaped pores according to the IUPAC classification. The abrupt closing of the desorption isotherm at a relative pressure of 0.45–0.5 was also observed and can be attributed to the cavitation phenomenon. All the remaining samples show type II adsorption isotherms (Fig. 5(b) and (c)) with unrestricted monolayer-multilayer adsorption, which appears to increase asymptotically when relative pressure (P/P_0) approaches one. This adsorption/desorption behaviour confirms the macroporous or nonporous nature of the particles.[46]

3.4 XPS

X-ray photoelectron spectroscopy (XPS) was performed to investigate the surface elemental composition, and the chemical states of the elements present in the different materials prepared in this work. Fig. 6 displays the results of XPS measurements for the nanoparticles synthesized with varying reaction pH (left-hand side) and varying reaction temperature (right-hand side). The survey spectra for synthesized nanoparticles (Fig. 6(a) and (b)) indicate that the samples consist of Bi, I, O and C indicating their high purity. The C 1s region was fitted with the standard three components C–C, C–O and (C═O)–C following common practice.[47] The samples show only one broad peak, and there are no known overlaps with other detected elements. Thus, carbon can be excluded from the analysis.

Fig. 6(c–h) show high-resolution spectra of Bi 4f, I 3d, and O 1s, respectively. Two significant peaks in the Bi region at binding energies of 158 eV and 163 eV are assigned to Bi $4f_{7/2}$ and Bi $4f_{5/2}$, respectively, which are characteristic of Bi^{3+}.[48,49] The binding energy of the Bi $4f_{7/2}$ core level remained between 157.9 and 158.1 eV across all samples (Fig. 6(c) and (d)). This variation in core level binding energies is small and is much less than what would be expected if second phases were present. It can be explained by small changes in the bonding environment of Bi^{3+} as the surface composition changes.[50]

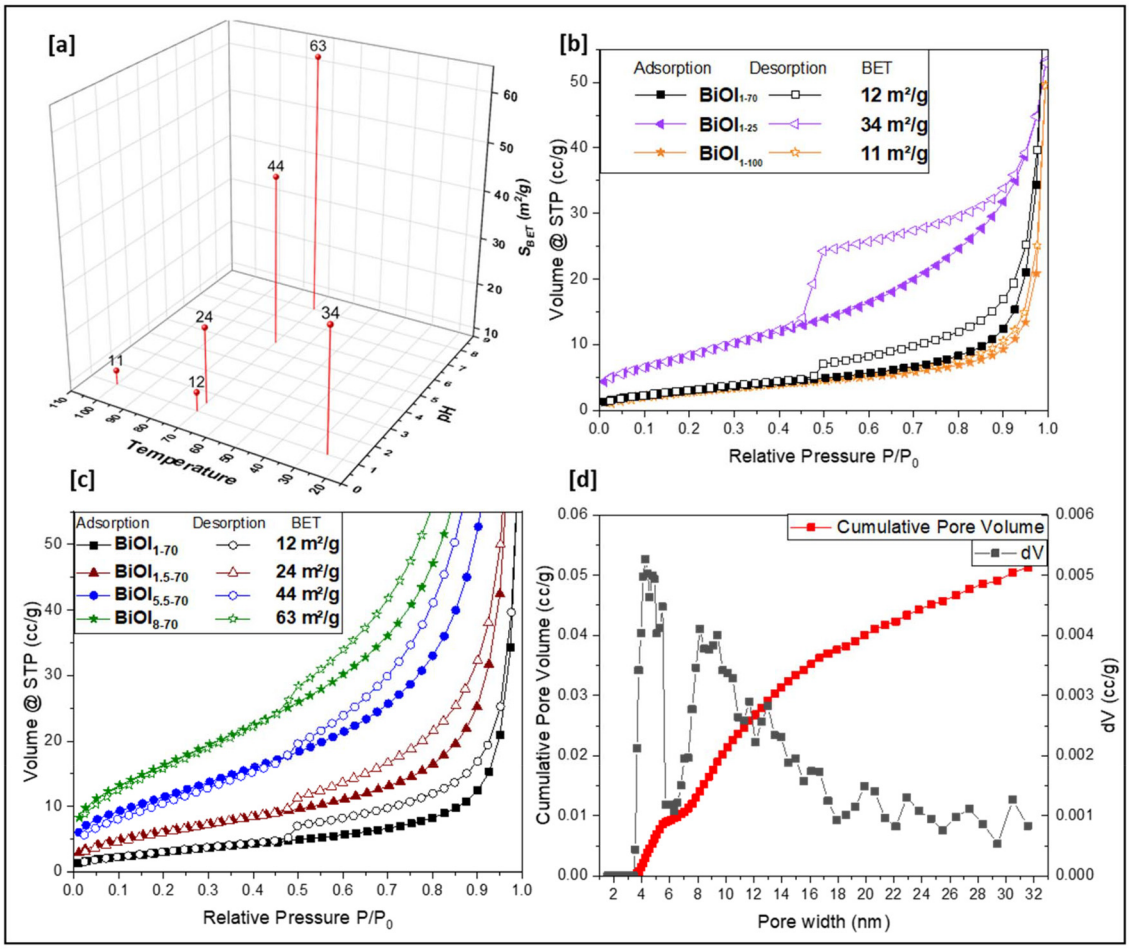

Fig. 5 Effect of change in pH and temperature (b) on S_{BET} (a). Adsorption–desorption isotherms with change in temperature (b), with change in pH (c) and pore size distribution of the particles $BiOI_{1-25}$ (d).

When the difference in binding energy between Bi $4f_{7/2}$ and I $3d_{5/2}$ is calculated, the values are almost constant. Here, the I $3d_{5/2}$ peak is used as a reference and fixed at 618 eV. The spectra of both Bi 4f and I 3d have simple, single-peak shapes. This shows that the I 3d peak represents very little change in binding energy (Fig. 6(e) and (f)). The oxygen O 1s peak of the samples consists of at least three components at binding energies of 529 eV, 531 eV, and 533 eV, respectively. The peak at the binding energy of 529 eV could be linked to lattice oxygen in BiOI. However, the source of the peaks at binding energies of 531 eV and 533 eV is not well documented.[50] Previous studies have reported their attribution to adsorbed organic contaminants, or other oxide/oxyhalide species (Bi_5O_7I, $Bi_7O_9I_3$, Bi_2O_3 *etc.*), or I–O bonds,[51] or Bi–OH bonds[35] or defect oxygen vacancies, or chemisorbed oxygen.[32,52] Changes in the O 1s peaks (Fig. 6(g) and (h)), especially in samples $BiOI_{8-70}$ and $BiOI_{1-100}$, show that variation in reaction pH and temperature affect the formation of these species in different ways. The intensity of the peak at 533 eV also demonstrates diverging trends with increasing reaction pH and temperature (Fig. S7, SI).

Surface elemental composition of the samples shows that the bismuth atomic percentage remained consistent with increasing reaction pH and temperature, while an increase in the oxygen component and decrease in the iodine component was observed. The decreasing iodine percentages with increasing reaction pH and temperature correspond with the EDX results. Fig. S7 in the SI shows a comparison of the iodine-to-bismuth ratio obtained from XPS and EDX measurements. Since XPS is a surface-sensitive technique, whereas EDX is used for bulk analysis, the higher iodine-to-bismuth ratio in the XPS readings indicates higher iodine content at the particle surface than in the bulk, which was observed with increasing reaction pH. In contrast, particles synthesized at higher reaction temperatures show a lower iodine-to-bismuth ratio in the XPS readings compared to the EDX readings, indicating a higher bismuth content at the surface.

3.5 UV-vis DRS

Optical properties of the synthesized products were assessed using UV-vis diffuse reflectance spectroscopy (DRS) and the

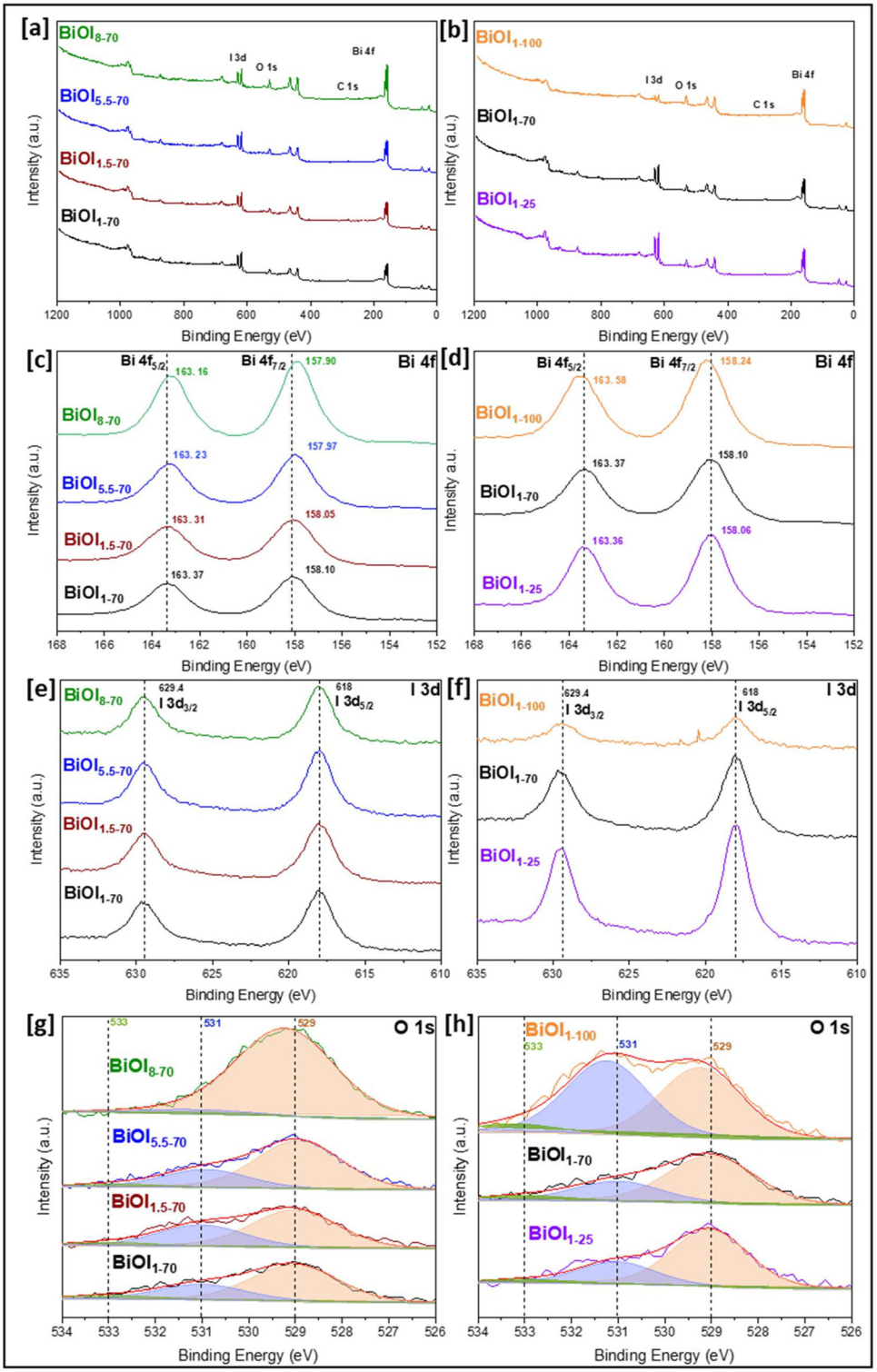

Fig. 6 XPS spectra of the synthesized nanoparticles. Survey (a, b), Bi 4f (c, d), I 3d (e, f), and O 1s (g, h).

results are depicted in Fig. 7. All the synthesized particles show strong absorption in the visible spectrum with absorption edges lying between 600 nm and 700 nm. Nanoparticles prepared at lower temperature without NaOH ($BiOI_{1-25}$, and $BiOI_{1-70}$) exhibit sharp and well-defined absorption edges, whereas $BiOI_{1-100}$ and particles synthesized under varying pH conditions display broader and more gradual absorption profiles (Fig. 7(a) and (c)) suggesting extended absorption in the longer wavelength region (NIR), possibly due to the formation of defects during synthesis.[53,54] Furthermore, the bandgap

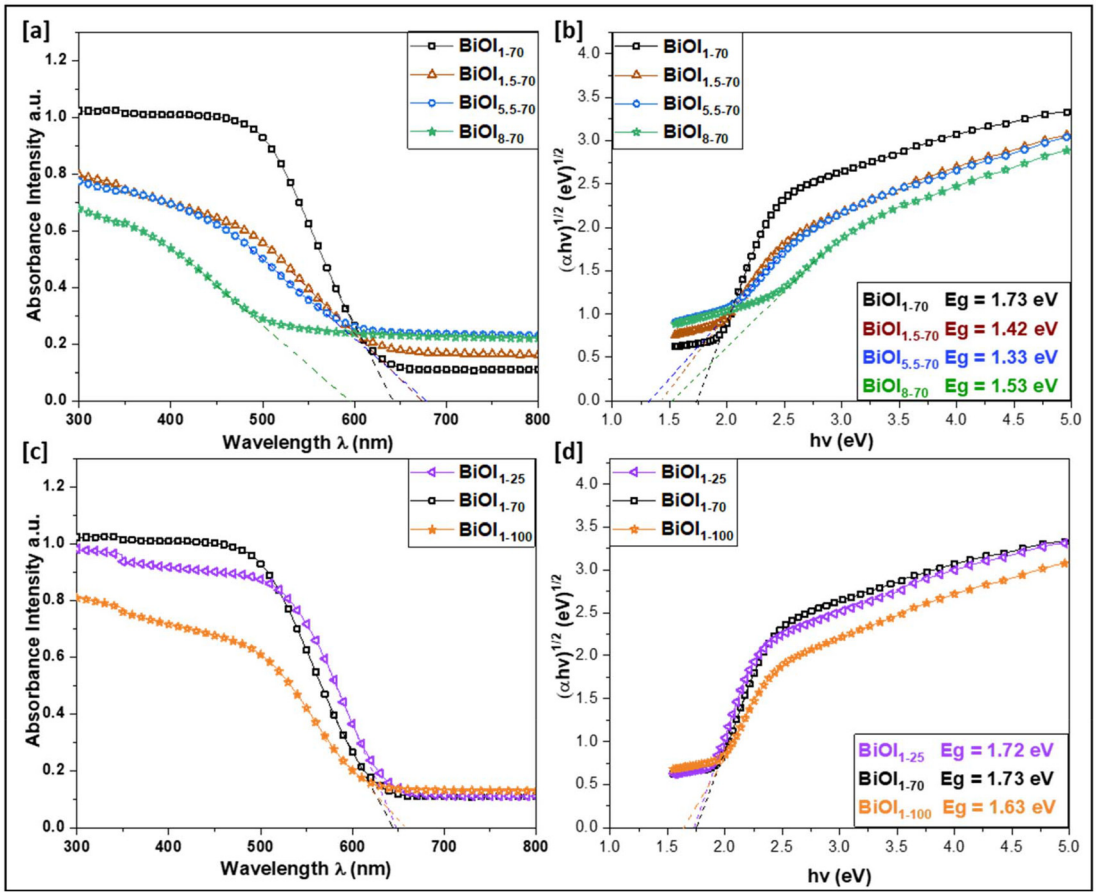

Fig. 7 Absorbance spectra and bandgap energy (E_g) of the samples synthesized with changing pH (a, b), and with changing temperature (c, d).

energy (E_g) values of the synthesized particles were determined using the Tauc expression shown below:

$$\alpha(h\nu) = A(h\nu - E_g)^{n/2}$$

where, α, ν, E_g, and A are the absorption coefficient, light frequency, bandgap energy, and a constant, respectively. The parameter n is determined by the type of electronic transition occurring in the semiconductor. For semiconductor materials with non-radiative transitions (*e.g.* BiOI), n is typically assigned a value of 4, indicating an indirect allowed transition. The bandgap energy (E_g) of the synthesized samples thus can be estimated using a Tauc plot, where $(\alpha h\nu)^{1/2}$ was plotted against photon energy ($h\nu$). The x intercept of the tangent drawn to the linear section of the curve provides a good approximation of the bandgap energy of the samples.[12] From Fig. 7(b) and (d) it is evident that the bandgap energies of all the samples are approximately 1.5 eV with particles $BiOI_{1.5-70}$ and $BiOI_{5.5-70}$ exhibiting the lowest bandgap energies of 1.42 eV and 1.33 eV, respectively.

3.6 Photocatalytic activity against BPA

Fig. 8 depicts the results of the photocatalytic batch experiment conducted to establish the photoactive performance of the various synthesized particles against BPA. All the synthesized particles except for $BiOI_{1-100}$ and $BiOI_{8-70}$ showed adsorption up to 7–8% of the initial concentration of BPA in the first hour of stirring in the dark. $BiOI_{8-70}$ displayed a slightly higher adsorption value of 10%, while $BiOI_{1-100}$ adsorbed only 3% of the initial concentration of BPA. This can be attributed to their respective specific surface areas. Particles synthesized at pH 1 and 70 °C ($BiOI_{1-70}$) showed around 60% degradation in the next 150 minutes under 50 W white LED irradiation. Increasing synthesis pH to 1.5 and 5.5 improved particle performance significantly, degrading 85% and 91% of BPA after 150 min under irradiation, respectively. However, a further increase in synthesis pH has produced particles ($BiOI_{8-70}$) with diminished photoactivity, resulting in 73% of BPA degradation (Fig. 8(a)).

Particles produced at 25 °C ($BiOI_{1-25}$) performed in a similar way to $BiOI_{1-70}$ for the first 30 minutes of irradiation. From that point onward, however, their degradation curves diverged, and $BiOI_{1-25}$ finally reached a BPA degradation rate of 45% after 210 minutes. $BiOI_{1-100}$ continued to perform poorly throughout the entire irradiation period, exhibiting a steady degradation curve with only 17% BPA degradation at the end of the experiment (210 min) (Fig. 8(c)).

Table 2 compares the results of photocatalytic activities of synthesized $Bi_xO_yI_z$ nanoparticles and their modified versions

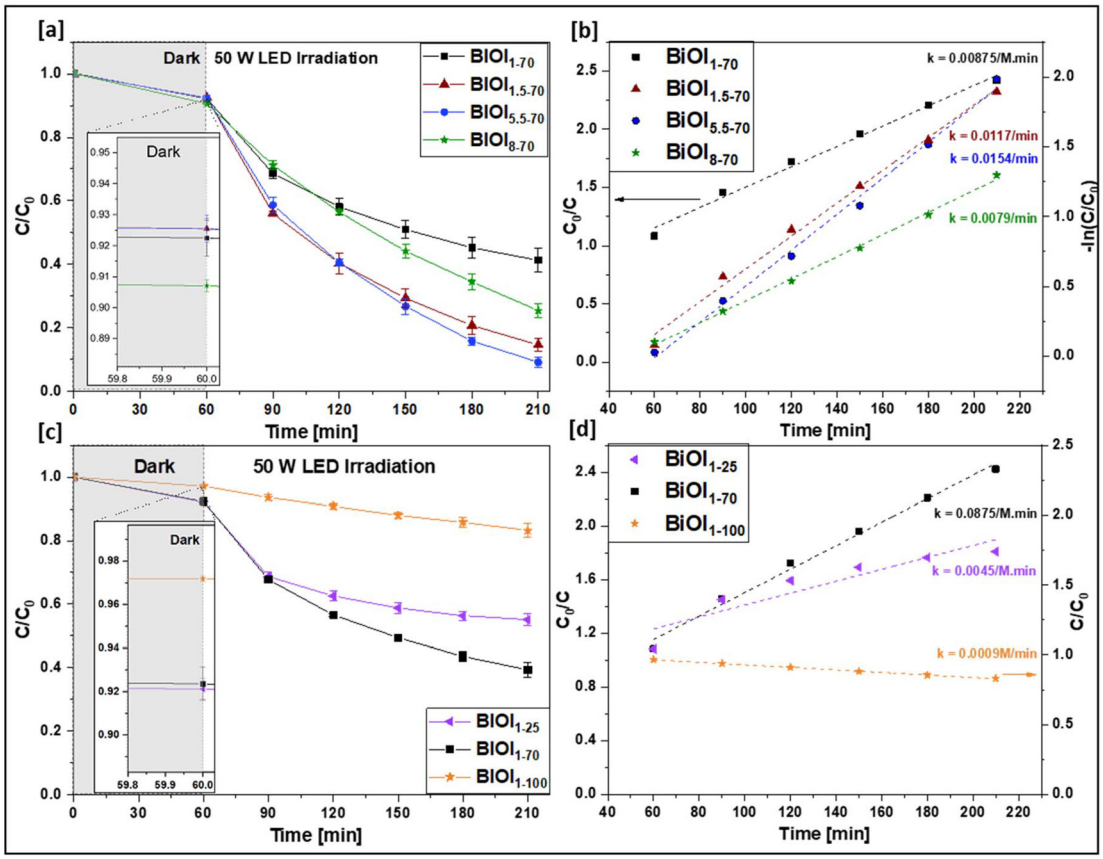

Fig. 8 Photocatalytic activity of particles against BPA and respective reaction rates according to pH (a, b), and temperature (c, d).

Table 2 Comparison of photocatalytic activities of $Bi_xO_yI_z$ nanoparticles against BPA

Product	C_0/C (mg g^{-1})	Irradiation source	$1-(C/C_0)$ (%)@t_{30}	Ref.
$BiOI_{1.5-70}$	30	50 W LED lamp	79	This work
$BiOI_{5.5-70}$	30	50 W LED lamp	73	This work
$Bi_7O_9I_3$	40	500 W I-W lamp	20	30
BiOI	10	500 W Xe lamp	20	55
BiOI + Bi nanodots	10	500 W Xe lamp	30	55
BiOI-001 facet	10	500 W Xe lamp	15	34
BiOI-110 facet	10	500 W Xe lamp	40	34
BiOI	8	24 W LED lamp	25	56
BiOI–Bi_2MoO_6	8	24 W LED lamp	35	56
BiOI	40	350 W Xe lamp	35	57
AgI–BiOI (1–8)	40	350 W Xe lamp	85	57
BiOI	33.33	35 W LED lamp	30	58
17.5% β-Bi_2O_3@BiOI	33.33	35 W LED lamp	65	58
BiOI	50	300 W Xe lamp	25	59
0.15 BiOI/ZnO nanorods	50	300 W Xe lamp	60	59
BiOI	20	500 W Xe lamp	50	60
GO@BiOI/Bi_2WO_6	20	500 W Xe lamp	40	60
BiOI	20	1000 W Xe lamp	50	61
$Bi_7O_9I_3$	10	50 W LED lamp	76	35
$Bi_7O_9I_3$	10	300 W Xe lamp	68	62
0.2 C_3N_4–$BiO_{1.2}I_{0.6}$	15	500 W Xe lamp	45	63

C_0/C_t is the initial amount of BPA per gram, per litre of catalyst loading. t_{30} is the percentage of the initial concentration of BPA degraded during the first 30 minutes of irradiation.

in various studies with $BiOI_{1.5-70}$ and $BiOI_{5.5-70}$. This comparison is focused on photocatalytic activity during the first 30 minutes of irradiation as we require a fast-acting product for our intended application in future work.

The photocatalytic performance of the synthesized nanoparticles primarily depends on the initial concentration of the model pollutant, the catalyst loading, and the source of irradiation used in the experiment. Employing BPA as a model pollutant, these nanoparticles are more effective when the ratio of initial BPA concentration to catalyst loading is lower (Fig. S8, SI). Furthermore, higher luminosity, achieved either through reflection (mirrored reactor) or the use of a higher power lamp, improves the results because a greater number of photons are available for photocatalysis (Fig. 12(b) and Fig. S9, SI).

Although the goal of this study was not to develop an optimal product, the BiOI nanoparticles synthesized here are, to the best of our knowledge, the most effective against BPA. Compared to other time-consuming and complex methods involving various heavy metal oxide heterojunction schemes, the simple and straightforward BiOI synthesis approach demonstrated in this work is not only significantly more efficient but also time-saving and environmentally friendly.

The reaction kinetics of heterogeneous catalysis, such as photocatalytic reactions in suspension-type systems, is often

described as following the Langmuir–Hinshelwood (L–H) mechanism[35,64] described by,

$$r_s = -\frac{dc}{dt} = k_s\theta_s = k_s\frac{k_d c}{1 + k_d c}$$

where r_s is the reaction rate, k_s is the reaction rate constant, θ is the surface coverage, k_d is the adsorption constant in the dark, and c is the reactant concentration.

In this work, the concentration of a reactant (BPA, 105 mg L^{-1}) is minimal compared to the amount of catalyst used (1 g L^{-1}). So, the value of product $k_d c$ is negligible with respect to unity. Hence, the above relationship can be described as pseudo-first-order kinetics and can be expressed as,

$$-\ln\frac{c_0}{c} = k_{app}t$$

where c_0 is the initial concentration (mg L^{-1}), k_{app} is the rate constant (min^{-1}), and t is the reaction time (min)

However, from Fig. 8((a), and (c)), it is observed that the degradation curves can be segregated into three types. Particles fabricated at different pH values ($BiOI_{1.5-70}$, $BiOI_{5.5-70}$, $BiOI_{8-70}$) show steady degradation curves, and can be fitted well in the above-mentioned pseudo-first-order reaction kinetics model with regression coefficients (R^2) > 0.99, while the remaining products, except for $BiOI_{1-100}$, exhibit diminishing photoactivity as the reaction progresses and can be fitted well with the second-order kinetics equation. $BiOI_{1-100}$ manifests a linear degradation curve indicating zero-order kinetics (Fig. S10, SI).

Reaction kinetics in such cases can be a function of many parameters, including the adsorption behaviour of BPA on the surface of catalytic particles, formation of intermediate products during the reaction, the generation and recombination rate of electron–hole pairs, and deterioration of the photocatalytic ability of the particles with time.[65,66] The results obtained so far indicate that, in addition to the surface area (S_{BET}) and bandgap energy (E_g), many other factors significantly influence the photocatalytic activity of the particles (Fig. 5–8). The measured total organic carbon content (TOC) in the reaction mixture also follows the degradation pathway of BPA with little quantitative difference, suggesting the absence of persistent by-products (Fig. S11, SI). All the product particles (except for $BiOI_{1-100}$) reveal a reaction order of greater than one, indicating that the reaction rate is influenced by more than one parameter despite using 10 times more catalyst than pollutant. There is also a possibility of multiple reaction orders during the various phases of reaction time. Hence, it is a challenging task to determine the degradation mechanism and a separate study is required to understand and model the reaction kinetics. However, for simple understanding, the calculated rate constants of the degradation reactions according to their fitting order are depicted in Fig. 8((b), and (d)). $BiOI_{5.5-70}$ demonstrated the best degradation rate with pseudo-first-order kinetics (k = 0.0154 min^{-1}), while $BiOI_{1-100}$ displayed the least activity with zero-order kinetics (k = 0.0009 M min^{-1}).

Based on the results above, it is evident that the product synthesized at lower temperature without the addition of NaOH ($BiOI_{1-25}$) exhibits minimal photocatalytic activity and does not show significant iodine loss. Therefore, further characterization studies are to be focused on comparing the mechanisms of iodine loss induced by pH and temperature, as well as their impact on photocatalytic performance.

3.7 FTIR spectroscopy

The presence of various functional groups and chemical bonds formed during the synthesis of $Bi_xO_yI_z$ nanoparticles was investigated by Fourier transform infrared (FTIR) spectroscopy. Fig. 9 shows the FTIR spectra of the synthesized particles.

All the particles show strong peaks around 1200 cm^{-1} to 1500 cm^{-1}, which is characteristic of the NO_3^- group.[67] This confirms the presence of unreacted bismuth nitrate or basic bismuth nitrate compounds in the synthesized nanoparticles. The broad peak around 3400 cm^{-1} and a sharp peak around 1620 cm^{-1} were attributed to the bending (δ(O–H)) and stretching (ν(O–H)) frequencies for the hydroxyl group.[68] Although all samples show a peak at around 3400 cm^{-1}, particles synthesized with varying pH display peaks of higher intensities. $BiOI_{5.5-70}$, which exhibits the highest photoactivity against BPA, also demonstrates the strongest peak intensity for the presence of the hydroxyl group. The presence of the hydroxyl group plays a vital role in defining the photocatalytic activity of the material as it can serve as an anchor to the contaminant molecules.[69,70] $BiOI_{1-70}$ shows a strong peak at around 1620 cm^{-1} (Fig. 9(b)), which can be associated with adsorbed water molecules on the surface. The vibration modes observed between 500 cm^{-1} and 1200 cm^{-1} originate from various phases of Bi–OH and Bi–O–Bi compounds.[67] These characteristic bands confirm the presence of hydroxyl and bismuth oxygen bonding environments suggesting their surface attachment or incorporation in the BiOI crystal structure. This leads to the formation defects that ultimately influence the photocatalytic and electronic properties of synthesized nanoparticles.

3.8 Raman and PL spectroscopy

To gather structural information concerning crystallinity and surface defects, Raman spectra of the samples were recorded at three different positions on each sample, and the analysis was completed using averaged spectra. Fig. 10(a) shows Raman spectra of the synthesized samples. $BiOI_{1-100}$ reveals characteristic vibrational peaks at 86 cm^{-1} and 149 cm^{-1} that are attributed to A_{1g} and E_g phonon stretching modes of Bi–I moieties, while substantial shifts of peak positions observed for the other samples suggested crystal lattice distortions.[30,71] The most intense peak signal at 96 cm^{-1} and shoulder peaks extending up to 150 cm^{-1} are most likely attributed to surface and interfacial defects caused by disruption of the lattice periodicity and the crystal structure.[45,72]

Photoactive products $BiOI_{5.5-70}$ and $BiOI_{1.5-70}$ exhibit an intense Raman peak at 96 cm^{-1} along with multiple shoulder

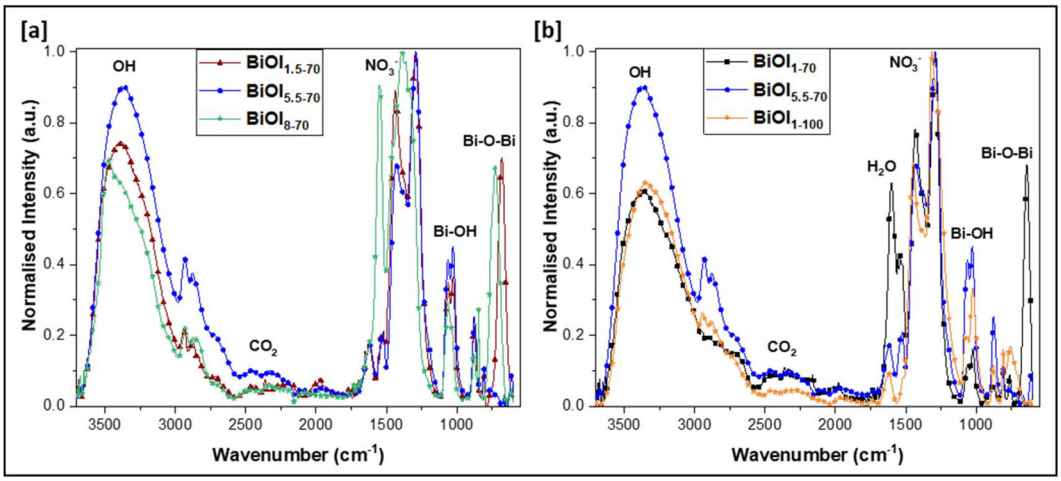

Fig. 9 FTIR spectra of nanoparticles synthesized with change in pH (a). Nanoparticles with highest and lowest photoactivity compared with $BiOI_{1-100}$ (b).

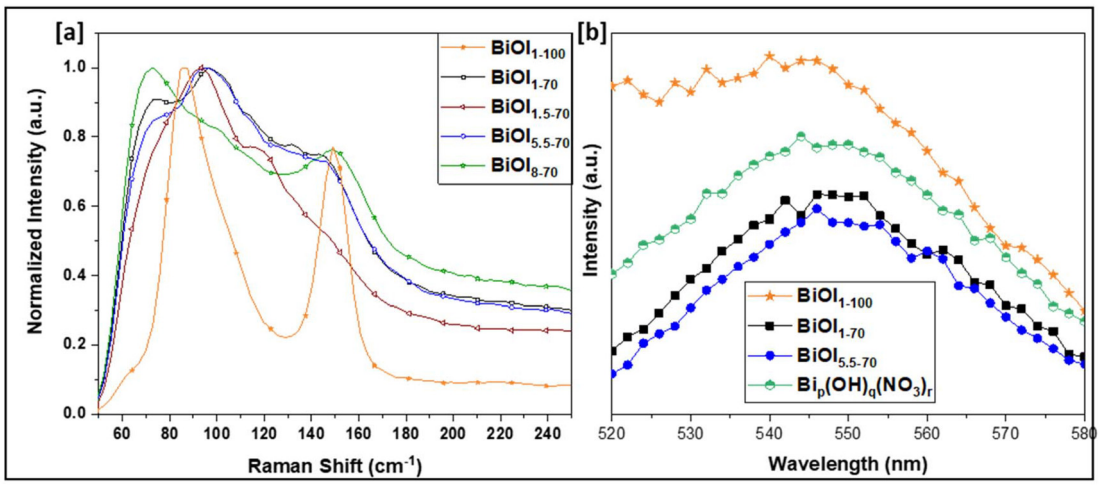

Fig. 10 Raman spectra (a) and photoluminescence (PL) spectra (b) of synthesized $Bi_xO_yI_z$, samples.

peaks up to 150 cm^{-1}. In contrast, although $BiOI_{8-70}$ featured a broader range of shoulder peaks extending up to 250 cm^{-1}, the relatively weak intensity of peaks within the 100 cm^{-1} to 150 cm^{-1} range suggested a lower concentration of the specific defect types present in $BiOI_{5.5-70}$ and $BiOI_{1.5-70}$. Notably, $BiOI_{1-100}$ lacks any apparent defect-related features in this spectral region, which correlates with its poor photocatalytic activity. While $BiOI_{1-70}$ exhibits a Raman profile similar to that of the more photoactive samples, its reduced photocatalytic performance may therefore be attributed to its lower specific surface area and the absence of surface hydroxyl (OH^-) groups, which play a crucial role in anchoring contaminant molecules.

In order to verify the efficiency of carrier separation in the particles formed *via* synthesis under varying pH and temperature conditions, photoluminescence (PL) spectra of $BiOI_{1-70}$, $BiOI_{5.5-70}$, $BiOI_{1-100}$, and white powder ($Bi_p(OH)_q(NO_3)_r$) were recorded. Lower PL intensity indicates more efficient interfacial charge migration and lower recombination of photogenerated electron–hole pairs.[73,74] As illustrated in Fig. 10(b), a strong PL peak can be found for particles prepared at the higher reaction temperature ($BiOI_{1-100}$), while the peak intensity is lowest for $BiOI_{5.5-70}$, revealing better separation of photogenerated carriers. Thus, the PL results agree with the results of the photoactivity shown by the respective particles. Notably, the peak intensity of the white powder was found to be higher than that of both $BiOI_{1-70}$ and $BiOI_{5.5-70}$, indicating its poor charge separation efficiency compared with the photoactive powders.

3.9 TEM analysis

Transmission electron microscopy (TEM) was employed to further analyse the crystal microstructure and embedded impurities in the synthesized samples. Fig. 11 shows the TEM images of the synthesized nanoparticles. $BiOI_{1-70}$ reveals a ten-

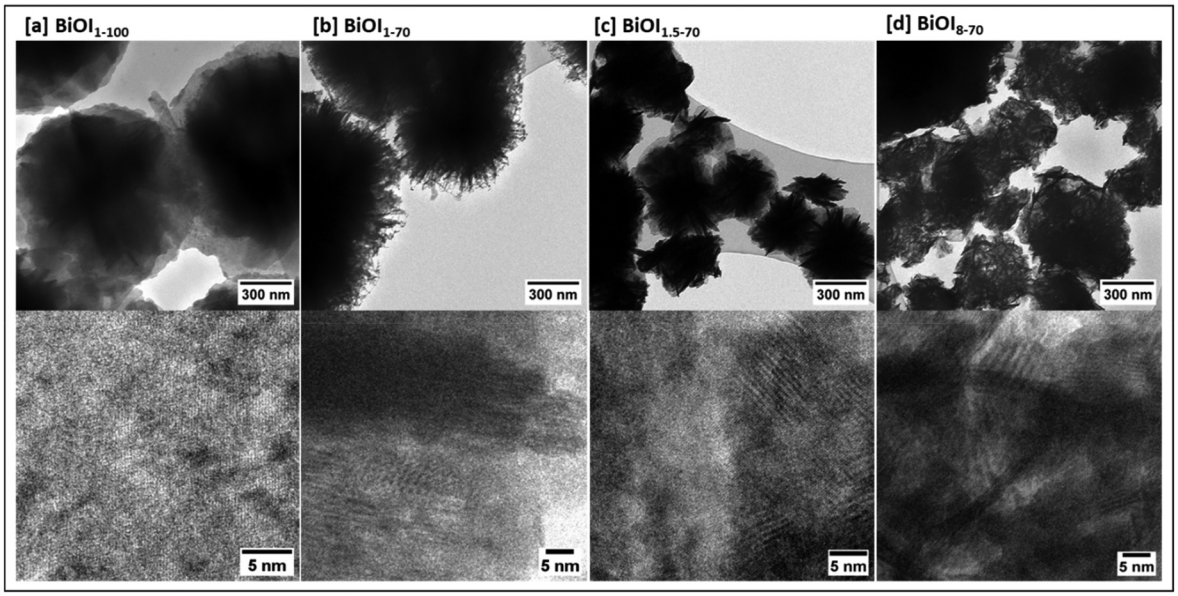

Fig. 11 TEM images (a–d) of synthesized $Bi_xO_yI_z$, nanoparticles.

tacle-like structure (Fig. 11(b) top). As the pH increases, these tentacles become thicker, while the particle size decreases and the structure becomes increasingly hollow (Fig. 11(c and d) top). The sintering of crystal granules at high reaction temperatures may contribute to the collapse of these tentacles and the formation of a more homogeneous structure in $BiOI_{1-100}$ (Fig. 11(a) top). Although, bismuth oxide compounds have been formed in all cases, $BiOI_{1-100}$ shows few signs of impurities being present in its polycrystalline form (Fig. 11(a) bottom). In contrast, samples synthesized at higher pH values display a mixture of crystalline orientations with varying lattice fringe spacings (Fig. 11(c and d) bottom), indicating increased structural disorder and formation of crystal defects. To further analyse the performance of the product ($BiOI_{5.5-70}$) exhibiting the best observed photocatalytic activity against BPA, the following experiments were conducted.

3.10 Molybdenum triiodide test

The spectrophotometric molybdenum triiodide method was employed to investigate the effect of catalyst loading and irradiation intensity on the formation of reactive oxygen species (ROS) during the first 30 minutes of irradiation.[75,76] To facilitate the test, 15 mL of 0.1 M potassium biphthalate aqueous solution was added to 15 mL of a mixture containing 0.4 M KI, 0.06 M NaOH and 0.0002 M sodium molybdate, and 20 mL of DI water. Various amounts of $BiOI_{5.5-70}$ powder were added to this 50 mL mixture and irradiated for 30 minutes to observe the following reaction (eqn (4)):

$$3I^- + H_2O_2 + 2H^+ \rightarrow I_3^- + 2H_2O \quad (4)$$

Photocatalytic water splitting occurred, leading to the formation of hydrogen peroxide, which eventually turned iodide ions into triiodide. The reaction mixture turned from colourless to yellow and an absorbance peak was observed at a wavelength of 350 nm. The results (Fig. 12(a)) indicate that increasing the catalyst loading leads to higher levels of ROS generation. However, the rate at which ROS increases with respect to catalyst loading is relatively low, which could eventually limit the effectiveness of further catalyst additions. Conversely, the rate of ROS formation increases more significantly with greater irradiation intensity, suggesting that greater light intensity could enhance pollutant degradation (Fig. 12(b)).

The photocatalytic activity of $BiOI_{5.5-70}$ against tetracycline (a model pharmaceutical) and rose bengal (a model dye) is presented in Fig. 12(c) and (d), respectively. Tetracycline exhibited ~35% adsorption on the photocatalyst within the first 15 minutes in the dark, while rose bengal showed significantly higher adsorption (~88%) under the same conditions. Minimal additional adsorption during the following 15 minutes indicates a rapid initial adsorption process. Upon light irradiation, further concentration decreases were observed, resulting in concentration reduction of up to 85% for tetracycline in 150 minutes and 99% for rose bengal in 60 minutes. These results demonstrate the high photocatalytic efficiency and broad applicability of $BiOI_{5.5-70}$ for the removal of diverse water pollutants.

3.11 Formation mechanism of the particles and its effects on particle photoactivity

It can be deduced from the overall results that the iodine atoms in the BiOI structure are very loosely bound and can be easily replaced by OH^- ions with increasing pH and temperature. Increasing the pH during particle synthesis (samples $BiOI_{1.5-70}$, $BiOI_{5.5-70}$, $BiOI_{8-70}$) results in particles with lower iodine content. Simultaneously, the photocatalytic activity of these particles increases compared to the sample produced at pH 1.

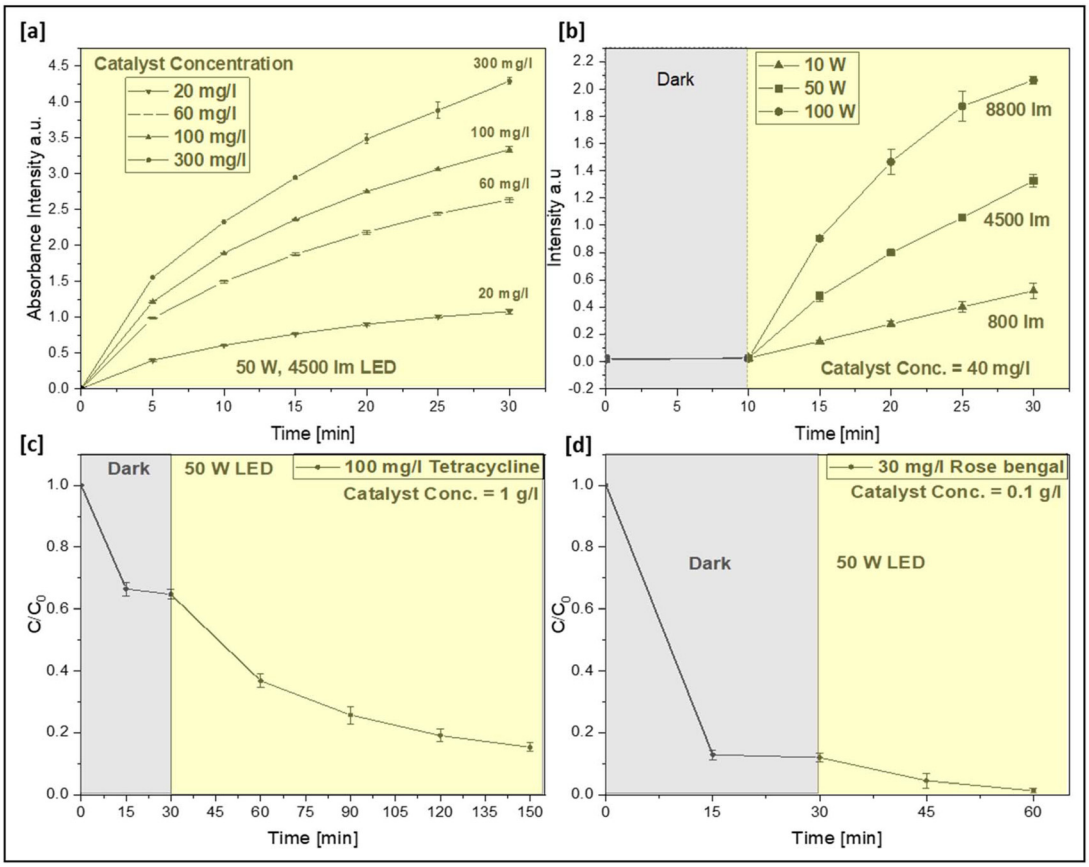

Fig. 12 Results of the molybdenum triiodide test with varying catalyst loading (a), and with varying irradiation intensity (b). Photocatalytic activity against tetracycline (c), and against rose bengal (d).

However, the reduced iodine content did not culminate in improved performance for $BiOI_{1-100}$. The absence of OH^- ions that induce defect formation and yield particles with low specific surface area (S_{BET}) could be a possible reason determining the limited photoactivity of $BiOI_{1-100}$. A comparison of the zeta potentials of $BiOI_{1-25}$, $BiOI_{1-70}$, $BiOI_{1-100}$, and $BiOI_{5.5-70}$ at around pH 6 did not reveal significant differences (Fig. S12, SI) and thus cannot be considered a determining factor defining the photoactivity of the synthesized nanoparticles. The bandgap energy, a critical parameter governing semiconductor performance, was consistently estimated to be around 1.5 eV across all the synthesized nanoparticles. Despite this similarity, significant variations in photocatalytic activity were observed, suggesting that the recombination of photogenerated electron–hole pairs plays a dominant role in determining photocatalytic efficiency. Notably, the formation of hydroxyl (OH^-)-induced defects when increasing the synthesis pH affects the internal electric field (IEF) of the BiOI crystal by changing its electron effect.[77] This eventually leads to an improvement in IEF and promoting the effective separation of photogenerated charges.[78] The defect-mediated suppression of recombination contributes to the enhanced photocatalytic activity observed for $BiOI_{1.5-70}$ and $BiOI_{5.5-70}$.

The authors believe that the difference between the particles produced with and without increasing pH (by using NaOH) arises mainly due to the formation of bismuth hydroxide ($Bi(OH)_3$) first until pH 7 and bismuth oxide (Bi_2O_3) afterwards, along with bismuth oxyiodide.[38,79] It is a well-known fact that bismuth nitrate pentahydrate ($Bi(NO_3)_3{\cdot}5H_2O$) can be converted to bismuth oxide (Bi_2O_3) with increasing pH through the formation of bismuth hydroxide ($Bi(OH)_3$) as an intermediate, which is stable up to pH 7. The possible formation mechanism, as shown in Fig. 13(a), is a very simplified approach, where nitrate (NO_3^-) groups are also present in the reaction mixture, competing for Bi^{3+} cations along with OH^- and I^-.[80] The iodine-to-bismuth ratios of the particles synthesized in this work fall in the range between 0.5 and 1, thus strengthening the mechanism described above. Furthermore, the presence of nitric acid also hinders the attachment of iodide to the bismuth cation, leading to a drop in the I : Bi ratio (see eqn (2) and (3)).

Particles synthesized under similar reaction conditions as $BiOI_{5.5-70}$ but without the addition of KI, yielded a white powder whose SEM images and XRD diffractograms resembled those of $BiOI_{5.5-70}$ and $BiOI_{8-70}$ (Fig. S5, SI). These results prove the dominance of these by-products at higher pH values.

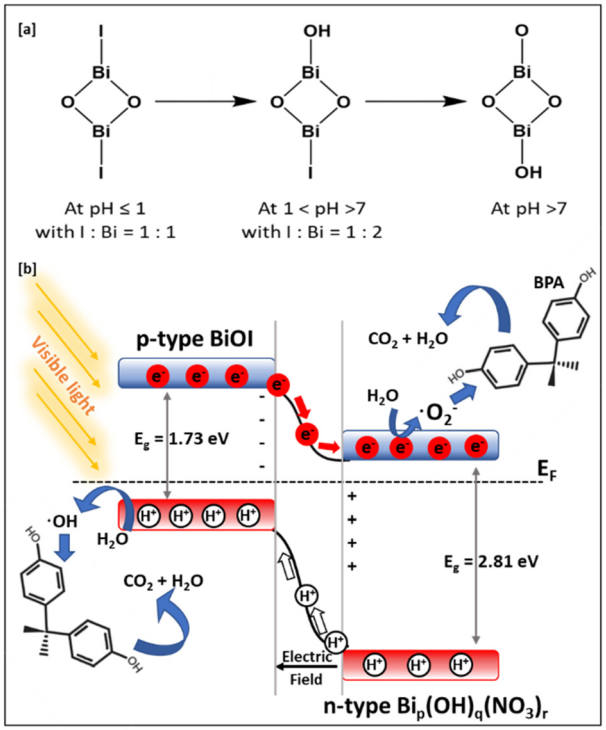

Fig. 13 Possible particle formation mechanism and energy band diagram.

However, this powder exhibited a very small surface area of 2 m^2 g^{-1} (Fig. S5, SI) and a nonporous or macroporous structure. Therefore, it can be stated that the introduction of iodide (KI) into the reaction mixture leads to the formation of a hierarchical structure, resulting in particles with larger surface areas. UV-vis DRS spectra of the white powder showed strong absorption below 400 nm, indicative of its activity in the UV light region. The bandgap energy was determined as 2.81 eV (Fig. S13(a and b), SI). The white powder exhibited no photoactivity under the same reaction conditions, and its physical mixture with pure $BiOI_{1-70}$ did not show any significant improvement in performance (Fig. S13(c), SI). Therefore, the enhanced performance of $BiOI_{1.5-70}$ and $BiOI_{5.5-70}$ can be attributed to the synergistic heterojunction effect between the two components rather than to a simple additive contribution of their individual photocatalytic activities. The Fourier transform infrared (FTIR) spectrum of this powder reveals at 1300 cm^{-1} and at 3400 cm^{-1} the presence respectively of nitrate (NO_3^-) and hydroxy (OH^-) groups in its structure (Fig. S13(d), SI). Fig. 13(b) shows the possible formation of a p–n heterojunction between p-type BiOI and n-type white powder ($Bi_p(OH)_q(NO_3)_r$), which could be responsible for interfacial band bending and the development of an internal electric field (IEF) that effectively suppresses charge recombination.[81,82] The heterojunction interface also reduces the resultant bandgap by allowing inter-material optical transitions, thereby broadening the spectral response into lower energy regions. This collectively results in the improvement of photocatalytic activity observed in the composite system of BiOI and $Bi_p(OH)_q(NO_3)_r$.

4. Conclusions and outlook

The novel solvo-hydrothermal method employed in this research not only yields a superior product but also offers a simplified approach for iodine reduction and defect generation to improve the oxidising ability of the synthesized particles and reduce the recombination of photoinduced charges, respectively. This innovative method streamlines the synthesis, making it more efficient and easily scalable, as it does not require the use of autoclaves, long reaction times, high temperatures, and addition of any metals or heavy metal oxides. It was illustrated that the structural formation and the direction of growth of $Bi_xO_yI_z$ flowerballs are notably influenced by critical factors such as pH and temperature. The 'pH induced' deficiency of iodide ions (I^-) restricts peripheral growth, while the 'temperature induced' deficiency hinders the inner growth of the flowerballs. In addition, it was demonstrated that synthesizing particles with a desirable surface area is feasible by targeted variations of pH and temperature. Moreover, optimal nanoparticle characteristics, along with enhanced overall quality and performance of the final product, were achieved through controlled optimization of the key variables in the synthesis procedure. All the synthesized products show some photoactivity towards BPA, but particles produced from the reaction mixtures under higher pH conditions exhibit superior performance. Defects formed due to the accumulation of OH^- in the crystal structure obstruct the recombination of charged carriers and thus improve the photocatalytic activity of the products. Photocatalytic experiments demonstrated that 0.1 g of $BiOI_{5.5-70}$ was able to degrade 9.6 mg of BPA during 150 minutes of irradiation. Accordingly, 1 g of $BiOI_{5.5-70}$ NPs have the capability to treat approximately 670 m^3 of water with an average BPA concentration of around 0.143 μg L^{-1},[83] further highlighting the efficiency of this technique. However, the kinetics of the reaction plays an important role in determining the viability of the intended scale-up and requires a separate study owing to its complexity. Furthermore, the solvent density and water content in the reaction mixture can also be crucial factors shaping the particle formation and, thus, need to be studied in detail. All in all, their low synthesis cost, narrow bandgap energy, which enables activity under low-cost visible light, and intensive photocatalytic properties, make $Bi_xO_yI_z$ NPs promising candidates for use in water treatment facilities as modifiers of membranes, adsorbents, and fillers, thereby contributing to the further development of sustainable water treatment technologies.

Author contributions

Conceptualization: A. K.; formal analysis: A. K.; funding acquisition: J. M. H.; investigation: A. K., K. S., R. B., M. K., and

C. S.; visualization: A. K.; supervision: J. M. H. and A. L.; writing – original draft preparation: A. K.; writing – review and editing: A. L., J. M. H., K. S., R. B., H. T., and C. S. All authors have read and agreed to the published version of the manuscript.

Conflicts of interest

The authors declare no conflict of interest.

Data availability

The data supporting the findings of this study are available from the corresponding authors upon request. All requested data and SI will be promptly provided to qualified researchers. Supplementary information: additional details relevant to the study. See DOI: https://doi.org/10.1039/d5nr04061b.

Acknowledgements

This work was supported by ERA-NET Cofound SAB grant number 10076758 (project CaFeOx). The authors would like to express their sincere gratitude towards Dr Petr Formanek (IPF) for conducting TEM measurements, Ms Anja Caspari (IPF) for TOC and zeta potential measurements, Ms Franzisca Kucharczyk (IPF) for PL measurements, and Dr Muhannad Al Aiti (TUD) for a helpful discussions.

References

1 CE_Consumer_Insights_2017.pdf, https://cosmeticseurope.eu/files/6114/9738/2777/CE_Consumer_Insights_2017.pdf (accessed August 8, 2023).
2 P. Gramatica, S. Cassani and A. Sangion, Aquatic ecotoxicity of personal care products: QSAR models and ranking for prioritization and safer alternatives' design, *Green Chem.*, 2016, **18**, 4393–4406, DOI: 10.1039/C5GC02818C.
3 A. Tauxe-Wuersch, L. F. De Alencastro, D. Grandjean and J. Tarradellas, Occurrence of several acidic drugs in sewage treatment plants in Switzerland and risk assessment, *Water Res.*, 2005, **39**, 1761–1772, DOI: 10.1016/j.watres.2005.03.003.
4 A. D. W. Tongue, S. J. Reynolds, K. J. Fernie and S. Harrad, Flame retardant concentrations and profiles in wild birds associated with landfill: A critical review, *Environ. Pollut.*, 2019, **248**, 646–658, DOI: 10.1016/j.envpol.2019.01.103.
5 T. T. Schug, A. Janesick, B. Blumberg and J. J. Heindel, Endocrine disrupting chemicals and disease susceptibility, *J. Steroid Biochem. Mol. Biol.*, 2011, **127**, 204–215, DOI: 10.1016/j.jsbmb.2011.08.007.
6 D. D. Seachrist, K. W. Bonk, S.-M. Ho, G. S. Prins, A. M. Soto and R. A. Keri, A review of the carcinogenic potential of bisphenol A, *Reprod. Toxicol.*, 2016, **59**, 167–182, DOI: 10.1016/j.reprotox.2015.09.006.
7 S. Hariganesh, S. Vadivel, D. Maruthamani and S. Rangabhashiyam, Disinfection by-products in drinking water: detection and treatment methods, in *Disinfection By-Products in Drinking Water*, Elsevier, 2020, pp. 279–304. DOI: 10.1016/B978-0-08-102977-0.00013-5.
8 C. M. Villanueva, Carcinogenicity of Disinfection Byproducts in Humans: Epidemiological Studies, in *Encyclopedia of Environmental Health*, Elsevier, 2019, pp. 517–527. DOI: 10.1016/B978-0-12-409548-9.11191-1.
9 M. Sillanpää and A. Matilainen, NOM Removal by Advanced Oxidation Processes, in *Natural Organic Matter in Water*, Elsevier, 2015, pp. 159–211. DOI: 10.1016/B978-0-12-801503-2.00006-9.
10 K. G. Linden and M. Mohseni, Advanced Oxidation Processes: Applications in Drinking Water Treatment, in *Comprehensive Water Quality and Purification*, Elsevier, 2014, pp. 148–172. DOI: 10.1016/B978-0-12-382182-9.00031-1.
11 K. P. Devi and H. Chaturvedi, An overview of nanotechnology in water treatment applications and combating climate change, in *Water Conservation in the Era of Global Climate Change*, Elsevier, 2021, pp. 191–212. DOI: 10.1016/B978-0-12-820200-5.00004-X.
12 X. Xiao and W.-D. Zhang, Hierarchical $Bi_7O_9I_3$ micro/nanoarchitecture: facile synthesis, growth mechanism, and high visible light photocatalytic performance, *RSC Adv.*, 2011, **1**, 1099, DOI: 10.1039/c1ra00323b.
13 S. Khan, J.-S. Park and T. Ishihara, A Review of the Single-Step Flame Synthesis of Defective and Heterostructured TiO2 Nanoparticles for Photocatalytic Applications, *Catalysts*, 2023, **13**, 196, DOI: 10.3390/catal13010196.
14 D. Kumar, S. K. Jat, P. K. Khanna, N. Vijayan and S. Banerjee, Synthesis, Characterization, and Studies of PVA/Co-Doped ZnO Nanocomposite Films, *Int. J. Green Nanotechnol.*, 2012, **4**, 408–416, DOI: 10.1080/19430892.2012.738509.
15 J. P. Guin, J. A. Sullivan, J. Muldoon and K. R. Thampi, Visible light induced degradation of perfluorooctanoic acid using iodine deficient bismuth oxyiodide photocatalyst, *J. Hazard. Mater.*, 2023, **458**, 131897, DOI: 10.1016/j.jhazmat.2023.131897.
16 A. Chachvalvutikul, J. Jakmunee, S. Thongtem, S. Kittiwachana and S. Kaowphong, Novel $FeVO_4/Bi_7O_9I_3$ nanocomposite with enhanced photocatalytic dye degradation and photoelectrochemical properties, *Appl. Surf. Sci.*, 2019, **475**, 175–184, DOI: 10.1016/j.apsusc.2018.12.214.
17 X. Lv, F. L. Y. Lam and X. Hu, A Review on Bismuth Oxyhalide (BiOX, X = Cl, Br, I) Based Photocatalysts for Wastewater Remediation, *Front. Catal.*, 2022, **2**, 839072, DOI: 10.3389/fctls.2022.839072.
18 D. S. Bhachu, S. J. A. Moniz, S. Sathasivam, D. O. Scanlon, A. Walsh, S. M. Bawaked, M. Mokhtar, A. Y. Obaid, I. P. Parkin, J. Tang and C. J. Carmalt, Bismuth oxyhalides:

synthesis, structure and photoelectrochemical activity, *Chem. Sci.*, 2016, **7**, 4832–4841, DOI: 10.1039/C6SC00389C.

19 S. Singh, R. Sharma and M. Khanuja, A review and recent developments on strategies to improve the photocatalytic elimination of organic dye pollutants by BiOX (X = Cl, Br, I, F) nanostructures, *Korean J. Chem. Eng.*, 2018, **35**, 1955–1968, DOI: 10.1007/s11814-018-0112-y.

20 X. Wei, M. U. Akbar, A. Raza and G. Li, A review on bismuth oxyhalide based materials for photocatalysis, *Nanoscale Adv.*, 2021, **3**, 3353–3372, DOI: 10.1039/D1NA00223F.

21 K. Sridharan, S. Shenoy, S. G. Kumar, C. Terashima, A. Fujishima and S. Pitchaimuthu, Advanced Two-Dimensional Heterojunction Photocatalysts of Stoichiometric and Non-Stoichiometric Bismuth Oxyhalides with Graphitic Carbon Nitride for Sustainable Energy and Environmental Applications, *Catalysts*, 2021, **11**, 426, DOI: 10.3390/catal11040426.

22 D. Jiang, L. Chen, J. Zhu, M. Chen, W. Shi and J. Xie, Novel p–n heterojunction photocatalyst constructed by porous graphite-like C_3N_4 and nanostructured BiOI: facile synthesis and enhanced photocatalytic activity, *Dalton Trans.*, 2013, **42**, 15726, DOI: 10.1039/c3dt52008k.

23 C. Chang, H. Yang, W. Mu, Y. Cai, L. Wang, L. Yang and H. Qin, In situ fabrication of bismuth oxyiodide ($Bi_7O_9I_3$/Bi_5O_7I) n-n heterojunction for enhanced degradation of triclosan (TCS) under simulated solar light irradiation, *Appl. Catal., B*, 2019, **254**, 647–658, DOI: 10.1016/j.apcatb.2019.05.030.

24 Q.-C. Liu, D.-K. Ma, Y.-Y. Hu, Y.-W. Zeng and S.-M. Huang, Various Bismuth Oxyiodide Hierarchical Architectures: Alcohothermal-Controlled Synthesis, Photocatalytic Activities, and Adsorption Capabilities for Phosphate in Water, *ACS Appl. Mater. Interfaces*, 2013, **5**, 11927–11934, DOI: 10.1021/am4036702.

25 H. Yu and Q. Han, Effect of reaction mediums on photocatalytic performance of BiOX (X = Cl, Br, I), *Opt. Mater.*, 2021, **119**, 111399, DOI: 10.1016/j.optmat.2021.111399.

26 J. C. Durán-Álvarez, C. Martínez, A. C. Mera, R. Del Angel, N. J. Gutiérrez-Moreno and R. Zanella, A Facile Synthetic Method to Obtain Bismuth Oxyiodide Microspheres Highly Functional for the Photocatalytic Processes of Water Depuration, *JoVE*, 2019, 59006, DOI: 10.3791/59006.

27 M. R. Elamin, K. H. Ibnaouf, N. Y. Elamin, F. A. Adam, A. H. Alolayan and B. Y. Abdulkhair, Spontaneous Adsorption and Efficient Photodegradation of Indigo Carmine under Visible Light by Bismuth Oxyiodide Nanoparticles Fabricated Entirely at Room Temperature, *Inorganics*, 2022, **10**, 65, DOI: 10.3390/inorganics10050065.

28 M. Long, P. Hu, H. Wu, Y. Chen, B. Tan and W. Cai, Understanding the composition and electronic structure dependent photocatalytic performance of bismuth oxyiodides, *J. Mater. Chem. A*, 2015, **3**, 5592–5598, DOI: 10.1039/C4TA06134A.

29 R. M. Matiur, A. A. Abuelwafa, S. Kato, N. Kishi and T. Soga, A comparative study on optical properties of BiOI, $Bi_7O_9I_3$ and Bi_5O_7I materials, *Opt. Mater.*, 2021, **111**, 110677, DOI: 10.1016/j.optmat.2020.110677.

30 P. Wu, L. Feng, Y. Liang, X. Zhang, X. Li, S. Tian, H. Hu, G. Yin and S. Khan, Large-scale synthesis of 2D bismuth-enriched bismuth oxyiodides at low temperatures for high-performance supercapacitor and photocatalytic applications, *J. Mater. Sci.: Mater. Electron.*, 2020, **31**, 5385–5401, DOI: 10.1007/s10854-020-03099-y.

31 G. Wu, Y. Zhao, Y. Li, H. Ma and J. Zhao, pH-dependent synthesis of iodine-deficient bismuth oxyiodide microstructures: Visible-light photocatalytic activity, *J. Colloid Interface Sci.*, 2018, **510**, 228–236, DOI: 10.1016/j.jcis.2017.09.053.

32 R. Ma, S. Zhang, X. Liu, M. Sun, J. Cao, J. Wang, S. Wang, T. Wen and X. Wang, Oxygen defects-induced charge transfer in $Bi_7O_9I_3$ for enhancing oxygen activation and visible-light degradation of BPA, *Chemosphere*, 2022, **286**, 131783, DOI: 10.1016/j.chemosphere.2021.131783.

33 R. He, J. Zhang, J. Yu and S. Cao, Room-temperature synthesis of BiOI with tailorable (0 0 1) facets and enhanced photocatalytic activity, *J. Colloid Interface Sci.*, 2016, **478**, 201–208, DOI: 10.1016/j.jcis.2016.06.012.

34 M. Pan, H. Zhang, G. Gao, L. Liu and W. Chen, Facet-Dependent Catalytic Activity of Nanosheet-Assembled Bismuth Oxyiodide Microspheres in Degradation of Bisphenol A, *Environ. Sci. Technol.*, 2015, **49**, 6240–6248, DOI: 10.1021/acs.est.5b00626.

35 D. Tuba-Guaman, M. Zuarez-Chamba, L. Quishpe-Quishpe, C. Reinoso, C. P. Santacruz, M. Herrera-Robledo and P. A. Cisneros-Pérez, Photodegradation of Rhodamine B and Bisphenol A Over Visible-Light Driven Bi_7O9I_3-and $Bi_{12}O_{17}Cl_2$-Photocatalysts Under White LED Irradiation, *Top. Catal.*, 2022, **65**, 1028–1044, DOI: 10.1007/s11244-022-01689-0.

36 L. Hu, H. Hu, W. Lu, Y. Lu and S. Wang, Novel composite $BiFeO_3/ZrO_2$ and its high photocatalytic performance under white LED visible-light irradiation, *Mater. Res. Bull.*, 2019, **120**, 110605, DOI: 10.1016/j.materresbull.2019.110605.

37 R. D. Rogers, A. H. Bond and S. Aguinaga, Alcoholysis of bismuth(III) nitrate pentahydrate by polyethylene glycols. Comparison with bismuth(III) nitrate crown ether complexation, *J. Am. Chem. Soc.*, 1992, **114**, 2960–2967, DOI: 10.1021/ja00034a031.

38 S. Liu, G. Ren, X. Gao, Z. Li, L. Wang and X. Meng, A novel bismuth hydroxide ($Bi(OH)_3$) semiconductor with highly-efficient photocatalytic activity, *Chem. Commun.*, 2022, **58**, 8198–8201, DOI: 10.1039/D2CC03369K.

39 K. Bogusz, D. Cardillo, M. Tehei, T. Boutard, P. J. Barker, T. Devers, A. Rosenfeld, S. X. Dou, H. K. Liu and K. Konstantinov, Biocompatible $Bi(OH)_3$ nanoparticles with reduced photocatalytic activity as possible ultraviolet filter in sunscreens, *Mater. Res. Bull.*, 2018, **108**, 130–141, DOI: 10.1016/j.materresbull.2018.08.041.

40 A. N. Christensen, M.-A. Chevallier, J. Skibsted and B. B. Iversen, Synthesis and characterization of basic

bismuth(III) nitrates, *J. Chem. Soc., Dalton Trans.*, 2000, 265–270, DOI: 10.1039/a908055d.

41 C. A. Abeledo and I. M. Kolthoff, The Reaction Between Nitrite and Iodide and its Application To The Iodimetric Titration of These Anions, *J. Am. Chem. Soc.*, 1931, **53**, 2893–2897, DOI: 10.1021/ja01359a008.

42 G. D. Robertson, D. M. Mason and W. H. Corcoran, The Kinetics of the Thermal Decomposition of Nitric Acid in the Liquid Phase, *J. Phys. Chem.*, 1955, **59**, 683–690, DOI: 10.1021/j150530a004.

43 Y.-C. Wu, Y.-C. Chaing, C.-Y. Huang, S.-F. Wang and H.-Y. Yang, Morphology-controllable Bi_2O_3 crystals through an aqueous precipitation method and their photocatalytic performance, *Dyes Pigm.*, 2013, **98**, 25–30, DOI: 10.1016/j.dyepig.2013.02.006.

44 S. A. Speakman, *Introduction to X-Ray Powder Diffraction Data Analysis*, 2013.

45 N. Sharma, Z. Pap, I. Székely, M. Focsan, G. Karacs, Z. Nemeth, S. Garg and K. Hernadi, Combination of iodine-deficient BiOI phases in the presence of CNT to enhance photocatalytic activity towards phenol decomposition under visible light, *Appl. Surf. Sci.*, 2021, **565**, 150605, DOI: 10.1016/j.apsusc.2021.150605.

46 M. Thommes, K. Kaneko, A. V. Neimark, J. P. Olivier, F. Rodriguez-Reinoso, J. Rouquerol and K. S. W. Sing, Physisorption of gases, with special reference to the evaluation of surface area and pore size distribution (IUPAC Technical Report), *Pure Appl. Chem.*, 2015, **87**, 1051–1069, DOI: 10.1515/pac-2014-1117.

47 G. Greczynski and L. Hultman, Undressing the myth of apparent constant binding energy of the C1s peak from adventitious carbon in X-ray photoelectron spectroscopy, *Sci. Talks*, 2022, **1**, 100007, DOI: 10.1016/j.sctalk.2022.100007.

48 Z. Zhao, F. Liu, L. Zhao and S. Yan, Preparation and XPS study of X-ray photochromic transparent BiOI/nylon11 composite film, *Appl. Phys. A*, 2011, **103**, 1059–1065, DOI: 10.1007/s00339-010-6038-9.

49 J.-M. Song, C.-J. Mao, H.-L. Niu, Y.-H. Shen and S.-Y. Zhang, Hierarchical structured bismuth oxychlorides: self-assembly from nanoplates to nanoflowers via a solvothermal route and their photocatalytic properties, *CrystEngComm*, 2010, **12**, 3875, DOI: 10.1039/c003497p.

50 T. N. Huq, L. C. Lee, L. Eyre, W. Li, R. A. Jagt, C. Kim, S. Fearn, V. Pecunia, F. Deschler, J. L. MacManus-Driscoll and R. L. Z. Hoye, Electronic Structure and Optoelectronic Properties of Bismuth Oxyiodide Robust against Percent-Level Iodine-, Oxygen-, and Bismuth-Related Surface Defects, *Adv. Funct. Mater.*, 2020, **30**, 1909983, DOI: 10.1002/adfm.201909983.

51 C. Chang, H. Yang, W. Mu, Y. Cai, L. Wang, L. Yang and H. Qin, In situ fabrication of bismuth oxyiodide ($Bi_7O_9I_3$/Bi_5O_7I) n-n heterojunction for enhanced degradation of triclosan (TCS) under simulated solar light irradiation, *Appl. Catal., B*, 2019, **254**, 647–658, DOI: 10.1016/j.apcatb.2019.05.030.

52 T. Jia, J. Wu, Z. Ji, C. Peng, Q. Liu, M. Shi, J. Zhu, H. Wang, D. Liu and M. Zhou, Surface defect engineering of Fe-doped $Bi_7O_9I_3$ microflowers for ameliorating charge-carrier separation and molecular oxygen activation, *Appl. Catal., B*, 2021, **284**, 119727, DOI: 10.1016/j.apcatb.2020.119727.

53 Y. He, Q. Lei, C. Li, Y. Han, Z. Shi and S. Feng, Defect engineering of photocatalysts for solar-driven conversion of CO_2 into valuable fuels, *Mater. Today*, 2021, **50**, 358–384, DOI: 10.1016/j.mattod.2021.03.021.

54 S. Khaled Mostaque, B. Kumar Mondal and J. Hossain, Theoretical insight into the enhancement of longer-wavelength light absorption in silicon solar cell with multilevel impurities, *Results Opt.*, 2022, **8**, 100250, DOI: 10.1016/j.rio.2022.100250.

55 S. Luo, J. Xu, Z. Li, C. Liu, J. Chen, X. Min, M. Fang and Z. Huang, Bismuth oxyiodide coupled with bismuth nanodots for enhanced photocatalytic bisphenol A degradation: synergistic effects and mechanistic insight, *Nanoscale*, 2017, **9**, 15484–15493, DOI: 10.1039/C7NR05320G.

56 M. Y. N. Núñez, M. Á. Rehlaender, A. Martínez-de La Cruz, A. Susarrey-Arce, F. M. Cuevas-Muñiz, M. Sánchez-Domínguez, T. E. Lara-Ceniceros, J. Bonilla-Cruz, A. A. Zapata, P. C. Hurtado, M. Pérez-Rodríguez, A. R. Orozco, L. T. González and F. E. Longoria-Rodríguez, Enhancing Visible Light Photocatalytic Degradation of Bisphenol A Using BiOI/Bi_2MoO_6 Heterostructures, *Nanomaterials*, 2023, **13**, 1503, DOI: 10.3390/nano13091503.

57 J. Lv, X. Liu, P. Li, W. Jin, J. Xu and Y. Zhao, AgI loading BiOI composites with enhanced photodegradation efficiency for bisphenol A under simulated solar light, *Sci. Total Environ.*, 2019, **669**, 194–204, DOI: 10.1016/j.scitotenv.2019.03.077.

58 S. Shu, H. Wang, Y. Li, J. Liu, J. Liu, J. Yao, S. Liu, M. Zhu and L. Huang, Fabrication of n-p β-Bi_2O_3@BiOI core/shell photocatalytic heterostructure for the removal of bacteria and bisphenol A under LED light, *Colloids Surf., B*, 2023, **221**, 112957, DOI: 10.1016/j.colsurfb.2022.112957.

59 C. Zhang, W. Fei, H. Wang, N. Li, D. Chen, Q. Xu, H. Li, J. He and J. Lu, p-n Heterojunction of BiOI/ZnO nanorod arrays for piezo-photocatalytic degradation of bisphenol A in water, *J. Hazard. Mater.*, 2020, **399**, 123109, DOI: 10.1016/j.jhazmat.2020.123109.

60 Z. Mengting, T. A. Kurniawan, Y. Yanping, R. Avtar and M. H. D. Othman, 2D Graphene oxide (GO) doped p-n type BiOI/Bi_2WO_6 as a novel composite for photodegradation of bisphenol A (BPA) in aqueous solutions under UV-vis irradiation, *Mater. Sci. Eng., C*, 2020, **108**, 110420, DOI: 10.1016/j.msec.2019.110420.

61 X. Xiao, R. Hao, M. Liang, X. Zuo, J. Nan, L. Li and W. Zhang, One-pot solvothermal synthesis of three-dimensional (3D) BiOI/BiOCl composites with enhanced visible-light photocatalytic activities for the degradation of bisphenol-A, *J. Hazard. Mater.*, 2012, **233–234**, 122–130, DOI: 10.1016/j.jhazmat.2012.06.062.

62 X. Xiao, R. Hao, X. Zuo, J. Nan, L. Li and W. Zhang, Microwave-assisted synthesis of hierarchical $Bi_7O_9I_3$ micro-

sheets for efficient photocatalytic degradation of bisphenol-A under visible light irradiation, *Chem. Eng. J.*, 2012, **209**, 293–300, DOI: 10.1016/j.cej.2012.07.142.

63 F. Mu, B. Dai, Y. Wu, G. Yang, S. Li, L. Zhang, J. Xu, Y. Liu and W. Zhao, 2D/3D S-scheme heterojunction of carbon nitride/iodine-deficient bismuth oxyiodide for photocatalytic hydrogen production and bisphenol A degradation, *J. Colloid Interface Sci.*, 2022, **612**, 722–736, DOI: 10.1016/j.jcis.2021.12.196.

64 R. Molinari, A. Caruso and L. Palmisano, Photocatalytic Processes in Membrane Reactors, in *Comprehensive Membrane Science and Engineering*, Elsevier, 2010, pp. 165–193. DOI: 10.1016/B978-0-08-093250-7.00039-6.

65 D. F. Ollis, Kinetics of Photocatalyzed Reactions: Five Lessons Learned, *Front. Chem.*, 2018, **6**, 378, DOI: 10.3389/fchem.2018.00378.

66 B. Ohtani, Photocatalysis by inorganic solid materials, in *Advances in Inorganic Chemistry*, Elsevier, 2011, pp. 395–430. DOI: 10.1016/B978-0-12-385904-4.00001-9.

67 Y. Astuti, A. Fauziyah, S. Nurhayati, A. D. Wulansari, R. Andianingrum, A. R. Hakim and G. Bhaduri, Synthesis of α-Bismuth oxide using solution combustion method and its photocatalytic properties, *IOP Conf. Ser.: Mater. Sci. Eng.*, 2016, **107**, 012006, DOI: 10.1088/1757-899x/107/1/012006.

68 P. Kamakshi, C. Joshitha, S. Chella and S. Selvaraj, Synthesis, characterization of BiOI/rGO nanocomposite and its photocatalytic functionality analysis under visible light, *Inorg. Chem. Commun.*, 2023, **150**, 110545, DOI: 10.1016/j.inoche.2023.110545.

69 A. C. Mera, Y. Moreno, D. Contreras, N. Escalona, M. F. Meléndrez, R. V. Mangalaraja and H. D. Mansilla, Improvement of the BiOI photocatalytic activity optimizing the solvothermal synthesis, *Solid State Sci.*, 2017, **63**, 84–92, DOI: 10.1016/j.solidstatesciences.2016.11.013.

70 D.-H. Wang, G.-Q. Gao, Y.-W. Zhang, L.-S. Zhou, A.-W. Xu and W. Chen, Nanosheet-constructed porous BiOCl with dominant {001} facets for superior photosensitized degradation, *Nanoscale*, 2012, **4**, 7780, DOI: 10.1039/c2nr32533k.

71 B. Long, Y. Huang, H. Li, F. Zhao, Z. Rui, Z. Liu, Y. Tong and H. Ji, Carbon Dots Sensitized BiOI with Dominant {001} Facets for Superior Photocatalytic Performance, *Ind. Eng. Chem. Res.*, 2015, **54**, 12788–12794, DOI: 10.1021/acs.iecr.5b02780.

72 L. Zeng, F. Zhe, Y. Wang, Q. Zhang, X. Zhao, X. Hu, Y. Wu and Y. He, Preparation of interstitial carbon doped BiOI for enhanced performance in photocatalytic nitrogen fixation and methyl orange degradation, *J. Colloid Interface Sci.*, 2019, **539**, 563–574, DOI: 10.1016/j.jcis.2018.12.101.

73 S. Zhang, S. Song, P. Gu, R. Ma, D. Wei, G. Zhao, T. Wen, R. Jehan, B. Hu and X. Wang, Visible-light-driven activation of persulfate over cyano and hydroxyl group co-modified mesoporous g-C_3N_4 for boosting bisphenol A degradation, *J. Mater. Chem. A*, 2019, **7**, 5552–5560, DOI: 10.1039/C9TA00339H.

74 Y. Yuan, R. Guo, L. Hong, Z. Lin, X. Ji and W. Pan, Fabrication of a dual S-scheme $Bi_7O_9I_3$/g-C_3N_4/Bi_3O_4Cl heterojunction with enhanced visible-light-driven performance for phenol degradation, *Chemosphere*, 2022, **287**, 132241, DOI: 10.1016/j.chemosphere.2021.132241.

75 P. Lockhart, B. K. Little, B. L. Slaten and G. Mills, Photogeneration of H_2O_2 in Water-Swollen SPEEK/PVA Polymer Films, *J. Phys. Chem. A*, 2016, **120**, 3867–3877, DOI: 10.1021/acs.jpca.6b00442.

76 B. K. Little, P. Lockhart, B. L. Slaten and G. Mills, Photogeneration of H_2O_2 in SPEEK/PVA Aqueous Polymer Solutions, *J. Phys. Chem. A*, 2013, **117**, 4148–4157, DOI: 10.1021/jp4021728.

77 J. Li, L. Cai, J. Shang, Y. Yu and L. Zhang, Giant Enhancement of Internal Electric Field Boosting Bulk Charge Separation for Photocatalysis, *Adv. Mater.*, 2016, **28**, 4059–4064, DOI: 10.1002/adma.201600301.

78 Y. Guo, W. Shi, Y. Zhu, Y. Xu and F. Cui, Enhanced photoactivity and oxidizing ability simultaneously via internal electric field and valence band position by crystal structure of bismuth oxyiodide, *Appl. Catal., B*, 2020, **262**, 118262, DOI: 10.1016/j.apcatb.2019.118262.

79 T. Zhang, X. Yue, L. Gao, F. Qiu, J. Xu, J. Rong and J. Pan, Hierarchically porous bismuth oxide/layered double hydroxide composites: Preparation, characterization and iodine adsorption, *J. Cleaner Prod.*, 2017, **144**, 220–227, DOI: 10.1016/j.jclepro.2017.01.030.

80 M. Bartoli, P. Jagdale and A. Tagliaferro, A Short Review on Biomedical Applications of Nanostructured Bismuth Oxide and Related Nanomaterials, *Materials*, 2020, **13**, 5234, DOI: 10.3390/ma13225234.

81 J. Jiang, H. Wang, X. Chen, S. Li, T. Xie, D. Wang and Y. Lin, Enhanced photocatalytic degradation of phenol and photogenerated charges transfer property over BiOI-loaded ZnO composites, *J. Colloid Interface Sci.*, 2017, **494**, 130–138, DOI: 10.1016/j.jcis.2017.01.064.

82 L. Wang, S. Sun, Z. Zhong, Q. Gong, X. Jiang, W. Zhou, L. Wang, M. Lin and Z. Yuan, Synthesis of $Bi_6O_6(OH)_3(NO_3)_3$·1.5H_2O/ZnO composite material with excellent photocatalytic hydrogen production performance, *Int. J. Smart Nano Mater.*, 2021, **12**, 185–197, DOI: 10.1080/19475411.2021.1933251.

83 S. M. Arnold, K. E. Clark, C. A. Staples, G. M. Klecka, S. S. Dimond, N. Caspers and S. G. Hentges, Relevance of drinking water as a source of human exposure to bisphenol A, *J. Exposure Sci. Environ. Epidemiol.*, 2013, **23**, 137–144, DOI: 10.1038/jes.2012.66.